ELSEVIER

Contents lists available at ScienceDirect

Ocean Engineering

journal homepage: www.elsevier.com/locate/oceaneng



Research paper

Coupled analysis and performance evaluation of a semi-submersible floating wind turbine with active ballasting system

Wei Meng ^[] a,b, Jiacan Lyu a,b, Yao Zhang c,*, Shangmao Ai ^[] a,b, Huanfeng Song ^d

- ^a Harbin Engineering University, 145 Nantong Street, Harbin, 150001, Heilongjiang Province, China
- b MIIT Key Laboratory of Deep-Sea Engineering Equipment and Technology, 145 Nantong Street, Harbin, 150001, Heilongjiang Province, China
- ^c University College London, Gower Street, London, WC1E 6BT, UK
- d China Ship Scientific Research Center, 185 Gaoxiong Street, Shanghai, 200011, China

ARTICLE INFO

Keywords: Floating wind turbine Computation fluid dynamics Potential-flow Semi-submersible platform Active ballasting system Coupled analysis TCP

ABSTRACT

Semi-submersible floating offshore wind turbines (FOWTs) are susceptible to platform inclination induced by wind thrust, which amplifies motion responses, reduces power generation efficiency, and compromises structural safety. To mitigate these challenges, an active ballasting system (ABS) can be introduced to dynamically redistribute the ballast water within the platform. A fully coupled aero-hydro-servo-elastic model is developed in SESAM, where the effects of ballast water movement are represented by applying external moments to the platform. Real-time interaction between the floating structure and the active ballasting program is established via TCP communication. The program, implemented in Python, employs a PID control algorithm based on platform pitch and roll angles, while incorporating pump flow constraints. The IEA 15 MW floating wind turbine is selected as the reference model. The coupled model is validated by comparing the motion responses of the FOWT without active ballasting against published benchmarks. Additionally, computational fluid dynamics (CFD) simulations are carried out to investigate the hydrodynamic behavior of the FOWT under both upright and inclined conditions. The active ballasting system is then applied in time-domain simulations under a range of environmental conditions. Simulation results demonstrate that the average inclination is reduced to near-zero, while the mean power output is improved under identical operating scenarios.

1. Introduction

The global energy crisis and growing environmental concerns have accelerated the expansion of wind power, which is expected to account for 28% of global electricity generation by 2050 (Eriksen et al., 2024). Compared to onshore wind energy, offshore wind offers distinct advantages, including higher and more consistent wind speeds, lower turbulence intensity, greater spatial availability, and reduced visual and noise pollution (Haider et al., 2024). Consequently, wind energy deployment is shifting toward deep-sea regions, with turbine structures evolving from fixed-bottom foundations to floating offshore wind turbines (FOWTs), making them a key focus for future development. Unlike fixed-bottom turbines, FOWTs rely on floating platforms to maintain stability and use mooring systems for station-keeping, making them more vulnerable to environmental forces such as turbulent winds, random waves, and tidal currents. These factors present significant challenges to system stability and operational efficiency. Overcoming these challenges necessitates a comprehensive understanding of FOWT dynamics and the integration of multidisciplinary design approaches to develop effective optimization strategies.

Meanwhile, as rotor diameters increase, the height of FOWTs also increases, amplifying dynamic effects due to their floating foundations (Edwards et al., 2023). This leads to larger tower-top displacements, raising the risk of fatigue, platform inclination, or capsizing (Gao et al., 2024). According to the Det Norske Veritas (DNV) design specifications (DNVGL-RP-0286) (Dnv, 2019), the maximum allowable tower-top acceleration for floating wind turbines in operation is 0.3 g, while the inclination angle should not exceed 10°. When FOWTs are in operation, the blades experience both lift and drag forces, driving rotor rotation while also being subjected to wind thrust. This thrust induces an average inclination angle on the windward side of the floating platform, affecting its hydrodynamic performance, power generation efficiency, and structural integrity. The effects of inclination angles on platform hydrodynamics were investigated through physical model experiments and frequency-domain numerical simulations (Amaral et al., 2021), where pitch motion was found to induce additional resonance responses due

E-mail address: yao.zhang@ucl.ac.uk (Y. Zhang).

^{*} Corresponding author.

to the inclination angle. Similarly, time-domain simulations were conducted to examine the nonlinear response of semi-submersible platforms with large inclination angles (Antonutti et al., 2016), and it was demonstrated that increased inclination significantly amplified motion amplitudes. From an aerodynamic perspective, platform pitch motion has been shown to reduce power output and increase blade stall risk (Wen et al., 2018), while computational fluid dynamics (CFD) studies further reveal that platform-induced aerodynamic load fluctuations and negative damping effects can amplify motion responses and impair efficiency (Feng et al., 2023). Under the combined influence of this average inclination and irregular wave excitation, the maximum pitch or roll angle of the platform may exceed the design safety limits, potentially resulting in reduced power performance or even triggering protective shutdown mechanisms. These findings underscore the critical impact of platform inclination on system performance and stability.

Therefore, mitigating platform motion is essential for ensuring the operational reliability and efficiency of FOWTs. Extensive research has been conducted on blade pitch control, nacelle and tower vibration mitigation, and platform motion control, exploring both active and passive strategies to improve overall system stability and performance.

Among these efforts, active blade pitch control remains a commonly explored strategy to regulate aerodynamic thrust and reduce platform motion (Wang et al., 2023), with the aim of improving power stability. The National Renewable Energy Laboratory (NREL) developed the open-source Reference OpenSource Controller (ROSCO) (Abbas et al., 2022), and simulation analyses on the NREL 5 MW and IEA 15 MW turbines showed that ROSCO could reduce maximum rotor thrust by over 10% and suppress platform pitch by up to 30%. Widely integrated into simulation tools such as FAST, Blade, and SESAM, ROSCO has provided a valuable foundation for subsequent pitch control research. Building on this, Gao et al. (2024) proposed a nonlinear pitch controller that maintained stable generator output under high wind speeds while effectively mitigating platform pitch motion. Comparative studies on the NREL FAST platform confirmed its advantages over conventional methods. Although the improved pitch strategy in ROSCO improves stability, it inevitably leads to power loss, highlighting the trade-off between load reduction and energy efficiency. As rotor sizes grow, pitch control becomes more challenging; Santos et al. (2022) showed that larger rotors prolong the natural pitch period, slowing control response and risking instability, highlighting the need for advanced strategies. Grant et al. (n.d.) investigated the integration of a parallel compensation blade pitch controller with low-bandwidth buoyancy-can ballasting using Open-FAST, showing that static ballasting and floating feedback control can act in synergy to reduce platform motion and structural loads.

In addition to blade pitch control, researchers have investigated nacelle and tower vibration reduction using tuned mass dampers (TMDs), a technique adapted from civil and mechanical engineering. Depending on the presence of control systems, these devices are categorized as passive TMDs or active mass dampers (AMDs. AMDs apply forces directly to the structure, offering improved control over dynamic responses (Zhang et al., 2025). Cai and Zhang (2021) and Zhang et al. (2023) demonstrated the effectiveness of passive TMDs in reducing pitch motion through numerical simulations and physical model tests, achieving up to 14.7 % pitch reduction. However, passive TMDs are sensitive to structural variations and lack robustness. To address this, He et al. (2020) proposed a hybrid damping system combining active and passive control, achieving a 20 % improvement in pitch suppression. Despite these advances, the large mass and space requirements of such systems limit their application in FOWTs.

Drawing inspiration from motion reduction strategies in offshore oil and gas platforms, heave plates are commonly adopted on semi-submersible FOWTs to enhance hydrodynamic damping (Wang et al., 2023). Li et al. (2024b) designed a dual-layer circular heave plate based on the OC4 DeepC wind platform and performed time-domain simulations using OpenFAST. The results showed that the additional mass and radiation damping in the heave and pitch directions were significantly

increased, leading to a reduction of approximately 5% in the average pitch angle. Lopez-Pavon and Souto-Iglesias (2015) conducted forced oscillation experiments on a column model equipped with heave plates, obtaining damping and added mass coefficients that were later used in time-domain simulations via Morison elements to account for viscous damping effects. They are also more sensitive to wave conditions and less effective in suppressing wind-induced quasi-static inclination.

Inspired by the mature ballasting systems used in conventional ship designs, researchers have explored the integration of active ballast control into floating wind turbine platforms. Existing ballast-based control strategies can be broadly divided into passive and active approaches. Passive ballast tanks essentially function as tuned liquid dampers (TLDs), where partially filled tanks reduce external excitations through sloshing-induced counteracting forces, with performance influenced by tank dimensions, liquid height, viscosity, and internal baffles (Dou et al., 2023). To overcome the frequency complexity and installation limitations of TLDs, tuned liquid column dampers (TLCDs) and tuned liquid multi-column dampers (TLMCDs) have been investigated. Zhang and eg (2020) placed TLCDs inside the nacelle of a spar-type turbine and found that uniform cross-sectional TLCDs performed better than non-uniform designs, especially when the wave frequency approached the natural pitch frequency of the platform. Xue et al. (2022) tested a semi-submersible turbine foundation with a TLMCD composed of three liquid columns and a connecting tube, showing that the device achieved optimal damping near resonance and reduced maximum pitch motion by 10.84% with only a 2% liquid mass ratio. Passive ballast tanks mainly reduce the amplitude of platform motions across different wave frequencies, representing a form of passive control strategy similar to heave plates, as both primarily target the suppression of wavefrequency responses.

Passive ballast tanks are effective in reducing platform motions at wave frequencies, contributing to improved hydrodynamic performance. At the same time, their ability to address the mean pitch induced by aerodynamic thrust is limited. Active ballast control complements this by enabling controlled redistribution of ballast water, which generates restoring moments to counteract the mean platform inclination. Roddier et al. (2010) introduced the concept of an active ballast tank in the design of the WindFloat foundation, using a dual-channel ballast pump capable of transferring up to 200 tons of water within 30 minutes to maintain positive floating stability. Mahfouz et al. (2021) developed an active ballast system for the ActiveFloat concrete semi-submersible platform, which effectively mitigated the aerodynamic negative damping effect and enabled smoother power output in time-domain simulations. Yu et al. (2022) conducted physical model tests of a floating wind turbine equipped with an active ballast adjustment system, and the experimental results closely matched numerical simulations, validating the feasibility of the system. Tetteh et al. (2022) explored the Ultraflexible Smart Floating Offshore Wind Turbine (USFLOWT) with its spiderFLOAT substructure, showing that active ballasting of buoyancy cans can rapidly adjust the mean heel angle, maintain near-zero pitch under both rated and extreme conditions, and thereby reduce component loads while maximizing power output. In contrast, Liu et al. (2023) proposed a turret-mounted FOWT design with a tailor-designed airfoilshaped A-frame tower that enables passive weathervaning, allowing the platform to align with wind direction without the need for an active yaw system or active ballast, thereby improving system reliability. Nanos et al. (2020) further explored the potential of active ballast control for vertical wake steering through wind tunnel tests and large eddy simulations. Their study revealed that this approach significantly altered wake characteristics, enhanced the inflow conditions of downstream turbines, and increased the total power output of a two-turbine array by approximately 8% under ideal conditions. Li et al. (2024a) developed a hydrostatic model based on the IEA 15 MW wind turbine to calculate the moment of inertia and hydrostatic coefficients of the platform during ballast transfer. The results showed that when the inclination angle remains below 15°, hydrodynamic coefficients from the positive floating

state remain applicable for simulation. Moreover, ballast transfer was found to improve average power output and reduce maximum nacelle acceleration, contributing positively to overall turbine performance.

In terms of ballasting control algorithms, Samyn et al. (2009) developed a six-degree-of-freedom dynamic model for semi-submersible platforms, taking into account the effects of ballast tank mass, moments, and inertia, providing a basis for ballast control system design. Manzi et al. (2005) proposed a control interface for ballast system operations on offshore drilling platforms, aiming to enhance ballast efficiency. Bara et al. (2012) formulated mathematical models incorporating vessel positioning, hull loads, and moments, and established an optimal control strategy for stable ballast regulation. Kurniawan et al. (2015) designed a PID-based ballast control system for catamarans. Liu et al. (2015) and Zhao et al. (2016) introduced a control method for a water-variable ballast chamber to improve control performance and reduce energy consumption. Horno et al. (2020) developed a dynamic model for a semi-submersible floating wind turbine and implemented a simplified nonlinear multivariable control system in the MATLAB-Orcaflex environment. Simulation results under various operating conditions confirmed the effectiveness of the proposed control algorithm. Hu et al. (2023) applied the AQWA software to analyze ship motion responses, and combined single-degree-of-freedom roll equations with vessel motion state equations. Using a model predictive control (MPC) strategy, they successfully reduced roll amplitude, demonstrating its applicability to time-domain motion control for marine structures.

Previous studies have demonstrated that integrating active ballast adjustment systems within floating platforms is an effective approach to mitigate wind turbine pitch motion. These investigations have primarily been conducted under the assumption of a positive floating condition, while limited attention has been given to the hydrodynamic behavior of the platform under inclined states. In addition, extensive research has focused on the design of ballast water distribution schemes and automatic control systems. Most of these studies are based on idealized control models and do not consider the influence of practical constraints, such as the limited capacity and dynamic response of ballast pumps during operation.

In this study, a potential-flow based approach is employed to simulate the hydrodynamic characteristics of a semi-submersible platform under wind-induced pitch moments. To validate the numerical method, CFD simulations based on the open-source software OpenFOAM are conducted, providing a comparison of the results for accuracy and reliability. In the following, real-time simulation of the ballast adjustment process is implemented by coupling SESAM software with an external control module via the Transmission Control Protocol (TCP). This setup enables the analysis of platform motion and power generation characteristics of a floating wind turbine under active ballast regulation, demonstrating the effectiveness of the potential-flow based approach combined with TCP for real-time ballast control.

The remainder of this paper is organized as follows. Section 2 introduces the numerical modeling approach, including the CFD model setup and the implementation of the active ballast system. Section 3 is the description of the floating offshore wind turbine used in this study. Section 4 analyzes the platform motion responses and power generation performance under different operational scenarios. Finally, Section 5 summarizes the key findings and outlines recommendations for future research.

2. Numerical methods

The primary numerical approach employed in this study is a fully coupled time-domain simulation based on potential-flow theory, implemented using the commercial software suite SESAM. This approach integrates aerodynamic forces, hydrodynamic loads, mooring dynamics, and control logic within a unified framework and serves as the primary tool for evaluating the dynamic behavior of FOWTs with the active ballasting

system (ABS), including long-term platform motions, power generation, mooring loads, and the performance of the active ballasting control.

In addition, a computational fluid dynamics (CFD) approach based on the Navier-Stokes equations is used as a complementary method. The CFD simulations aim to verify the validity of the upright platform assumption commonly adopted in potential-flow models by comparing the hydrodynamic responses of the semi-submersible platform under both upright and inclined conditions.

The following subsections provide detailed descriptions of both numerical methods.

2.1. Coupled solver for FOWT with ABS

To efficiently evaluate the dynamic response of FOWTs with active ballasting systems under combined wind and wave loading, this study primarily adopts SESAM, a fully coupled simulation framework based on potential flow theory. Within this framework, the WADAM module computes frequency-domain hydrodynamic coefficients, including added mass matrices, hydrostatic restoring force matrices, and first and second order wave excitation loads. As WADAM is based on potential-flow theory, it enables fast and accurate predictions of large-scale off-shore structures under wave conditions and has been widely applied in the offshore oil and gas industry (Dnv and Manual, 2023). The SIMA module performs fully coupled time-domain simulations by integrating wave-induced platform motions with the elastic responses of slender structural components such as blades, tower, and mooring lines.

As illustrated in Fig. 1, the FOWT model is constructed using the SIMA simulation environment. The platform, nacelle, and hub are modeled as rigid SIMO bodies (Dnv, 2023b), while the blades, tower, and mooring lines are represented using RIFLEX elements (Dnv, 2023a). The coupling of SIMO and RIFLEX modules allows for the simultaneous simulation of rigid body motions and the structural response of slender components. Their integration within the SIMA platform enables fully coupled time-domain dynamic analysis, which has been validated in previous studies (Kvittem and Moan, 2015).

To model the effect of ballast redistribution, the "External DLL Force" functionality in SIMA is employed to apply external control moments on the platform, mimicking the dynamic effects generated by active ballast system

An active ballasting program is developed in the Python environment. As Fig. 1 shown, the control program comprises modules for time-averaging the inclination angles, a proportional-integral-derivative (PID) controller for computing the desired control moment, and constraints reflecting the ballast pump capacity. Real-time communication between the active ballast program and the dynamic simulation is established via the SIMA simopy interface using the TCP. At each time step, SIMA provides the current pitch or roll angle to the control program. And the active ballasting program calculates the required moments and sends them back to SIMA for application. This real-time data exchange ensures synchronized operation and dynamic adjustment of the active ballasting system. The use of TCP ensures reliable communication, including features such as error detection, correction, and congestion control, making it well-suited for this integrated framework.

2.1.1. Equations of motion

The equations of motion are written as (Dnv, 2023b):

$$([m] + A_{\infty})\ddot{\mathbf{x}} + D\mathbf{f}(\dot{\mathbf{x}}) + K\mathbf{x} + \int_0^t h(t - \tau)\dot{\mathbf{x}}(\tau)d\tau = q(t, \mathbf{x}, \dot{\mathbf{x}})$$
(1)

with

$$h(\tau) = \frac{1}{2\pi} \int_{-\infty}^{\infty} c(\omega) + i\omega a(\omega) e^{i\omega t} d\omega$$
 (2)

where [m] is the body mass matrix, A_{∞} is the added mass matrix at infinite frequency, D is the damping matrix, $f(\dot{x})$ is the vector function where each element is given by $f_i = \dot{x}_i |\dot{x}_i|$, K is the hydrostatic stiffness matrix, $h(\tau)$ is the retardation function, is computed by a transform of

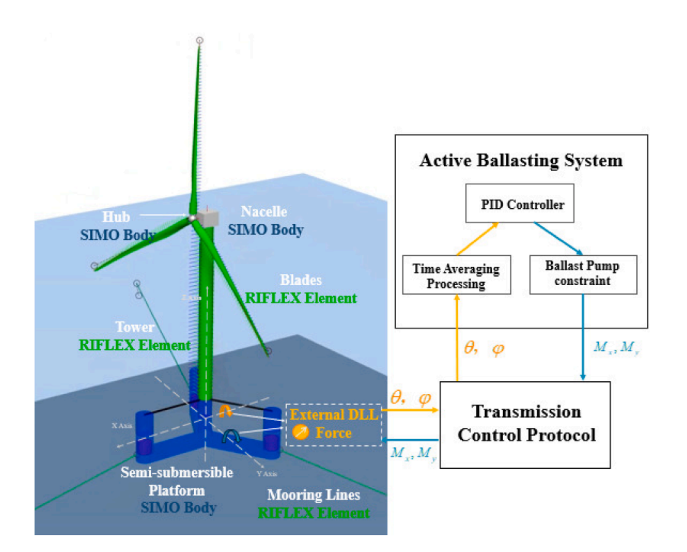


Fig. 1. Illustration of FOWT with active ballasting system in Sima.

the frequency-dependent added-mass $a(\omega)$ and damping $c(\omega)$, x is the position vector and q is the exciting force vector.

The exciting forces $q(t, \mathbf{x}, \dot{\mathbf{x}})$ on the right-hand side of Eq. (1) are given by

$$q(t, \mathbf{x}, \dot{\mathbf{x}}) = q_{wave} + q_{moor} + q_{aero} + q_{ballast}$$
(3)

where q_{wave} is the wave excitation force, q_{moor} is the restoring force of the mooring system, q_{aero} is the coupled force from tower and wind turbine caused by wind, and $q_{ballast}$ is external forces from ballast system.

In this study, the hydrostatic stiffness matrix K, the frequency-dependent added mass $a(\omega)$, and damping $c(\omega)$ are calculated by WADAM, before being given as input to the floater in SIMA. To consider the influence of viscous drag, the damping matrix provided in the reference study (Allen et al., 2020) is used.

2.1.2. Wave loads

The wave excitation force q_{wave} can be expressed by the following equation, where the two terms represent a Volterra series truncated after the quadratic term, as described by Hasselmann (1966) and Dalzell (1976).

$$q_{wave} = q_{wave}^{(1)}(t) + q_{wave}^{(2)}(t)$$
(4)

where $q_{wave}^{(1)}(t)$ and $q_{wave}^{(2)}(t)$ are the first-order and second-order wave excitation force

In this study, the first-order wave excitation and the second-order difference frequency forces are considered and can be calculated by the following formula, where the second-order wave forces are evaluated using the Newman method (Newman, 1974).

$$\begin{cases}
\mathbf{q}_{wave}^{(1)}(t) = \operatorname{Re} \sum_{m} \tilde{\xi}_{m} H^{(1)}(\omega_{m}) e^{i\omega_{m}t} \\
\mathbf{q}_{wave}^{(2)}(t) = \operatorname{Re} \sum_{m} \sum_{n} \tilde{\xi}_{m} \tilde{\xi}_{n}^{*} H_{mn}^{(2-)}(\omega_{m}, \omega_{n}) e^{i(\omega_{m} - \omega_{n})t}
\end{cases}$$
(5)

where $\tilde{\xi}_m$ is complex Fourier component of sea surface elevation with frequency ω_m , $H^{(1)}(\omega_m)$ is the first-order transfer function, $\tilde{\xi}_n^*$ is complex Fourier component of sea surface elevation with frequency ω_m , and $H_{mn}^{(2-)}(\omega_m,\omega_n)$ is the quadratic transfer functions for the difference-frequency force.

For semi-submersible platforms, the second-order difference frequency force is essential due to its dominance at low natural frequencies, which may align with the natural frequency of the platform-mooring system. The high-frequency sum-frequency force can be neglected because the response of the platform in that range is minimal. In this study, the first-order transfer function $H^{(1)}(\omega_m)$ and the quadratic transfer functions for the difference-frequency force $H_{mn}^{(2-)}(\omega_m,\omega_n)$ are also computed by WADAM first in the frequency domain.

2.1.3. Mooring system loads

The mooring system forces are computed using the RIFLEX component within the SIMA module, where mooring lines are modeled with finite elements. The structural analysis is based on the small strain approximation, which is particularly suitable for slender marine structures (Dnv, 2023a), and is grounded in well-established principles of continuum mechanics. For mooring elements without bending stiffness, spatial bar elements are formulated using a fully Lagrangian approach with integrated cross-sectional properties. Each element is assumed to remain straight, with a constant initial cross-sectional area along its length. The two nodes of each element possess three translational degrees of freedom, defined in the global coordinate system. Element length is tracked in both the undeformed and deformed configurations, enabling accurate representation of axial deformation under dynamic loading.

2.1.4. Aerodynamics loads

The aerodynamic load model used for wind turbines in RIFLEX and SIMO is based on the Blade Element Momentum (BEM) theory, which combines classical momentum theory with blade element theory (Dnv, 2023a). In this approach, each blade is discretized into multiple two-dimensional airfoil-shaped elements along its span. The fundamental principle is that the aerodynamic forces acting locally on each blade element–calculated using empirical lift and drag coefficients–are balanced with the change in momentum of the airflow passing through the rotor disk. Further details on BEM theory can be found in Manwell et al. (Manwell et al., 2010).

For each airfoil section, the aerodynamic loads are determined by interpolating from static lift, drag, and moment coefficient curves. The lift force per unit length is denoted as F_L , the drag force as F_D , and the aerodynamic moment as M. Wind velocity V_{Wind} and structural velocity $V_{\mathrm{Structure}}$ are computed at the center of each element, based on the undisturbed wind speed and the structural velocity at the corresponding nodes. The relative velocity V_r in the airfoil coordinate system is computed as:

$$V_r = V_{Wind} - V_{Structure} \tag{6}$$

The angle of attack α is computed based on the local V_{rx} and V_{ry} components of the velocity. The Reynolds number Re is computed as:

$$Re = \frac{\rho_{air}c\sqrt{\left(V_{r_x}^2 + V_{r_y}^2\right)}}{v_{air}} \tag{7}$$

where ρ_{air} is the air density, c is the chord length, and v_{air} is the viscosity of air

The forces and moment (about the airfoil coordinate system) per unit length are:

$$F_L = \frac{1}{2} C_L \rho_{\text{air}} c \left(V_{r_x}^2 + V_{r_y}^2 \right) \tag{8}$$

$$F_D = \frac{1}{2} C_D \rho_{\text{air}} c \left(V_{r_y}^2 + V_{r_y}^2 \right) \tag{9}$$

$$M = \frac{1}{2} C_M \rho_{\text{air}} c^2 \left(V_{r_x}^2 + V_{r_y}^2 \right) \tag{10}$$

where C_L , C_D and M are lift, drag and moment coefficients obtained by interpolation in the airfoil tables based on Re and α (Gaertner et al., n.d.)

 $F_L,\,F_D$ and M are multiplied by the length of the element, transformed into the appropriate coordinate system, and are applied to the nodes in a lumped manner. To account for unsteady aerodynamic effects, the present study incorporates the semi-empirical Beddoes-Leishman dynamic stall model, which captures the influence of dynamic stall and includes corrections for tip losses, hub losses, and skewed wake effects. The aerodynamic loads acting on the rotor blades are calculated using BEM theory. The aerodynamic influence of the tower is modeled separately using potential-flow theory, which simulates the tower shadow effect. These models are combined to support subsequent aeroelastic analysis under varying wind conditions.

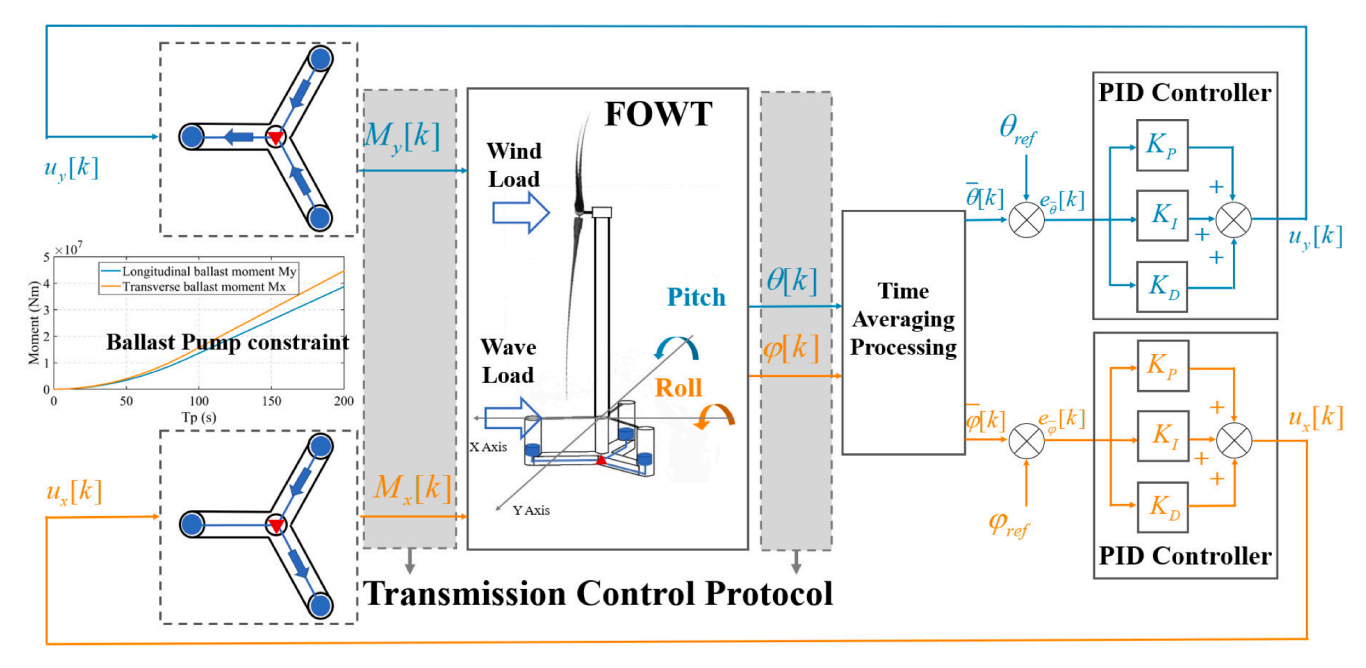


Fig. 2. Scheme of the signals flow between SIMA and active ballasting system.

In this study, turbulent wind fields are pre-generated using 64-bit TurbSim (Jonkman and Buhl, 2006), a stochastic wind field simulator developed by the NREL. The generated wind fields are used as inputs for the floating wind turbine simulations. Additionally, the Reference OpenSource Controller (ROSCO, version 2.6.0) is employed to regulate turbine operation during the simulations, ensuring optimal aerodynamic performance and system stability.

2.1.5. Coupled analysis of FOWT with ABS

Fig. 2 illustrates the coupling strategy employed in this study, integrating SIMA and active ballasting system via TCP. During each time step, SIMA provides the instantaneous pitch and roll angles $(\theta[k])$ and $\varphi[k]$ to the active ballasting system. After calculation, the active ballasting system returns the ballast moments $(M_x[k])$ and $M_y[k])$ constrained by the water pump.

The time moving averages are calculated by:

$$\bar{\varphi}[k] = \frac{1}{N} \sum_{n=k-N+1}^{k} \varphi[n] \tag{11}$$

$$\bar{\theta}[k] = \frac{1}{N} \sum_{n=k-N+1}^{k} \theta[n] \tag{12}$$

with sampling period $T_s = 0.01s$, where k represents the current time step and N represents the length of the averaging window.

The averaged errors are computed as:

$$e_{\bar{\varphi}}[k] = \varphi_{ref} - \bar{\varphi}[k] \tag{13}$$

$$e_{\bar{\theta}}[k] = \theta_{ref} - \bar{\theta}[k] \tag{14}$$

Then the required moments $u_x[k]$ and $u_y[k]$ can be calculated by PID controllers:

$$u_{x}[k] = K_{p,\varphi} e_{\bar{\varphi}}[k] + K_{i,\varphi} T_{s} \sum_{i=0}^{k} e_{\bar{\varphi}}[i]$$

$$+ K_{d,\varphi} \frac{e_{\bar{\varphi}}[k] - e_{\bar{\varphi}}[k-1]}{T_{s}}$$

$$(15)$$

$$u_{y}[k] = K_{p,\theta} e_{\bar{\theta}}[k] + K_{i,\theta} T_{s} \sum_{i=0}^{k} e_{\bar{\theta}}[i] + K_{d,\theta} \frac{e_{\bar{\theta}}[k] - e_{\bar{\theta}}[k-1]}{T_{s}}$$
(16)

where the proportional gain (K_p) generates a corrective moment proportional to the deviation between the average inclination and the target angle of the platform. The integral gain (K_i) accounts for sustained inclination deviations caused by persistent wind thrust, enhancing the regulation speed through integration. The derivative gain (K_d) helps suppress overshoot induced by the corrective moment.

In all simulations, a consistently tuned set of PID parameters is applied, with $K_p = 2 \times 10^5$, $K_i = 1 \times 10^3$, and $K_d = 1 \times 10^5$, used identically for both pitch and roll control. These values are determined through a systematic tuning process to balance responsiveness and stability. The large proportional gain provides strong corrective action, the small integral gain avoids long-term offsets, and the derivative gain damps transients. This configuration yields a rapid and stable response without overshoot, maintaining the platform inclination near zero under turbulent wind and irregular wave conditions.

The required moments $u_x[k]$ and $u_y[k]$ are subsequently constrained by the pump capacity limits, yielding the final implemented moments $M_x[k]$ and $M_y[k]$, which are applied to the platform within the same time step through the TCP communication protocol. Specifically, the pump exhibits a gradual increase in flow rate during startup until reaching its maximum capacity. Once the maximum flow rate is achieved, the ballast moment can only be adjusted at a limited rate in each time step, reflecting the maximum volume of water that can be transferred within that interval. After the target ballast moment is reached, the applied moment remains constant. In addition, the maximum achievable ballast moment is inherently constrained by the capacity of the ballast tanks.

2.2. Navier-Stokes solver

Although potential-flow methods can effectively predict motion responses under most operating conditions, they typically rely on the assumption that the platform remains upright and have limitations in capturing viscous flow effects. When the platform tilts under wind thrust, geometric nonlinearity and fluid viscosity may further influence its motion response (Antonutti et al., 2016). Most existing studies are based on upright platform conditions, with limited investigation into hydrodynamic behavior under inclined scenarios. To verify the applicability of potential-flow methods at small inclination angles, this study further employs computational fluid dynamics (CFD) based on the Navier—

Stokes (NS) equations. As the fundamental governing equations for viscous fluid motion, the NS equations comprehensively account for inertia, viscosity, and pressure variations. By comparing the hydrodynamic responses of the semi-submersible platform in both upright and inclined conditions, the CFD simulations confirm that the upright-platform assumption remains reasonable and valid under small-angle inclinations

In the viscous fluid domain, Ω_{CFD} , the flow field is solved by a two-phase incompressible viscous-flow solver. The flow is governed by the momentum equations

$$\frac{\partial(\rho \mathbf{U})}{\partial t} + \nabla \cdot (\rho(\mathbf{U} - \mathbf{U}_g)\mathbf{U}) - \nabla \cdot \mu \nabla \mathbf{U} - \nabla \mathbf{U} \cdot \nabla \mu
= -\nabla p_d - \mathbf{g} \cdot \mathbf{x} \nabla \rho$$
(17)

and the continuity equation

$$\nabla \cdot \mathbf{U} = 0 \tag{18}$$

where ρ is the fluid density, **U** is the flow velocity, **U**_g is the mesh velocity, μ is the dynamic viscosity, **g** is the gravitational acceleration, p_d the dynamic pressure, expressed by $p_d = p + \mathbf{g} \cdot \mathbf{x}$, p is the pressure, and $\mathbf{x} = (x, y, z)$ is coordinate of a point in the flow field.

In the present two-phase-flow model, the volume of fluid (VOF) method is applied to model the phase interface. An additional transport equation is solved for the volume fraction of the water phase, α_0 , by applying the Multidimensional Universal Limiter with Explicit Solution (MULES) method.

$$\frac{\partial(\alpha_0)}{\partial t} + \nabla \cdot (\mathbf{U}\alpha_0) + \nabla \cdot (\mathbf{U}_r\alpha_0(1 - \alpha_0)) = 0 \tag{19}$$

where **U** is the divergence-free velocity field, $\nabla \cdot (\mathbf{U}_r \alpha_0 (1 - \alpha_0))$ is an artificial compression term to suppress the interface smearing with \mathbf{U}_r the compression velocity (Deshpande et al., 2012).

The fluid density, ρ , and the dynamic viscosity, μ , in Eq. (17) are then calculated by the VOF values at the cell centers.

$$\rho = \alpha_0 \rho_0 + \alpha_1 \rho_1 \tag{20}$$

$$\mu = \alpha_0 \mu_0 + \alpha_1 \mu_1 \tag{21}$$

where the subscripts 0 and 1 denotes the water phase and the air phase, respectively, and ρ and μ are the fluid density and dynamic viscosity, respectively.

The above governing equations are solved by the finite volume method in OpenFOAM (Jasak, 1996). The pressure implicit with splitting of operators (PISO) algorithm (Issa, 1986) is employed for the velocity-pressure coupling. In the present work, the Crank-Nicolson scheme (blending factor 0.95) is applied for time marching, the linear upwind scheme and the linear scheme are adopted for the convection and diffusion terms, respectively.

The motions of the floating bodies are handled using the Laplacian mesh morphing technique in OpenFOAM (Jasak and Ž Tuković, 2010). The displacement of the rigid body boundaries is obtained by solving the equations of motion. The mesh deformation is then computed by solving a Laplacian equation (see Eq. (22)), so that the boundary conditions for the mesh motion are smoothly propagated to the mesh cells.

$$\nabla \cdot (\Gamma_c \nabla \mathbf{V}_c) = 0 \tag{22}$$

In the above equation, Γ_c is the mesh motion diffusivity coefficient, and \mathbf{V}_c is the mesh deformation vector field. In the present work, the inverse distance method is applied to define the diffusion coefficient.

3. Model description

The 15 MW FOWT model, released by the International Energy Agency (IEA) in 2020 and designed by the University of Maine, is adopted in this study. As an open-source reference model that has

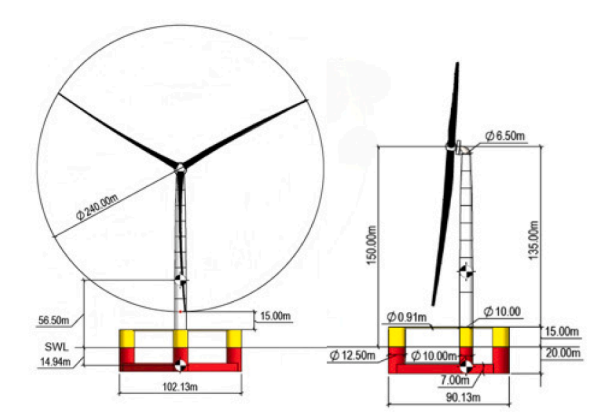


Fig. 3. FOWT model diagram Allen et al. (2020).

Table 1FOWT general system properties Allen et al. (2020).

Parameter	Units	Value
Turbine Rating	MW	15
Hub Height	m	150
Draft	m	20
Total System Mass	t	20093
Platform Mass	t	17 839
Tower Mass	t	1263
Rotor Nacelle Assembly Mass (RNA)	t	991
Water Depth	m	200
VCG of Platform	m	-14.94
VCG of Tower	m	56.50
I_{xx} of the Platform	$kg \cdot m^2$	1.25×10^{10}
I_{yy} of the Platform	$kg \cdot m^2$	1.25×10^{10}
I_{zz} of the Platform	$kg \cdot m^2$	2.36×10^{10}

Note: VCG denotes the vertical position of the center of gravity measured from the waterline.

been widely applied in prior research, it offers reliable data for validation and ensures consistency in evaluating the active ballasting system. As illustrated in Fig. 3, the platform consists of a four-column steel semi-submersible structure. Key system parameters are summarized in Table 1, with additional details available in the corresponding technical reports (Allen et al., 2020). The listed moments of inertia (I_{xx} , I_{yy} , and I_{zz}) correspond to the rotational inertia about the longitudinal (x), transverse (y), and vertical (z) axes of the platform, respectively. These values are defined with respect to the center of gravity of the platform and represent only the mass distribution of the platform itself, excluding contributions from other components in the overall system.

The mooring system layout is shown in Fig. 4. The configuration consists of three catenary lines, each 850 m in length, connected to the three outer columns of the platform via fairleads located 14 m below the still water level. The lines are arranged at 120° intervals and anchored to the seabed at a depth of 200 m. All the mooring lines are made of studless R3 chain with a nominal diameter of 185 mm. Fig. 4 also indicates the wind and wave directions used in subsequent simulation cases.

According to the corresponding technical reports (Allen et al., 2020), the total mass of the semi-submersible platform is 17 854 t, which includes 3914 t of structural steel and 2540 t of fixed iron ore-concrete ballast, evenly distributed at the base of the three outer columns. In addition, 11 300 t of seawater ballast are used to submerge most of the submerged pontoons, along with 100 t for the tower interface components. To enable active ballast adjustment, the seawater ballast is divided into two parts in this study: a fixed portion uniformly distributed within the submerged pontoons, and a variable portion located in dedicated ballast tanks inside the three outer columns. These tanks are interconnected by pipelines, and ballast water is transferred among them via ballast

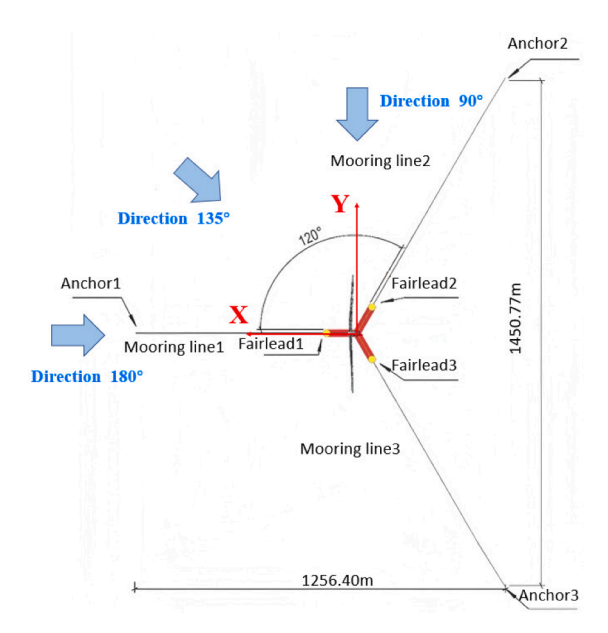


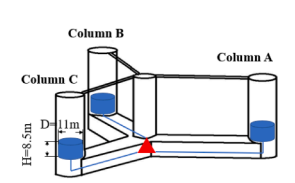
Fig. 4. Mooring system diagram Allen et al. (2020).

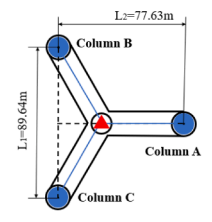
pumps, as illustrated in Fig. 5a. Each variable ballast tank has a base diameter of 11 m, a height of 8.5 m, and a volume of 807 m³, initially containing approximately 400 m³ of seawater. Transferring ballast water from columns B and C to column A induces longitudinal inclination, while transferring water from column B to column C causes lateral inclination. The corresponding equivalent displacement distance caused by ballast transfer is shown in Fig. 5b.

The variable ballast water in this study amounts to 1230 t, representing 6.12% of the total displacement. When ballast water is transferred from columns B and C to column A, the induced moment reaches the predefined upper limit of 5° pitch inclination. Under this condition, the center of gravity shifts 1.17 m along the x-axis and 0.05 m upward along the z-axis, corresponding to 1.30% of the platform length in the x-direction and 0.33% of the vertical center of gravity, respectively. The redistribution also changes I_{yy} and I_{zz} by 0.12%, indicating that the influence on center of gravity and inertia properties is minor. These findings are consistent with Li et al. (2024a), who showed that hydrodynamic coefficients obtained under upright-floating assumptions remain valid when inclination angles are below 15°. Therefore, representing ballast redistribution through an equivalent external moment is considered a reasonable simplification in hydrodynamic simulations.

The control moments generated by ballast redistribution, denoted as M_x and M_y , varying with the amount of water transferred and are also influenced by the pump flow characteristics. As shown in Fig. 6, the left axis represents the pump flow rate, while the right axis shows the corresponding control moment produced by the transferred ballast over time t_p , measured from pump activation. The pump reaches its maximum flow rate of $0.33\,\mathrm{m}^3/\mathrm{s}$ at 90 s, and the total transferred volume reaches $400\,\mathrm{m}^3$ at $1,200\,\mathrm{s}$, corresponding to the maximum control moment. Once the motion of the FOWT stabilizes after the adjustment process, the pump is turned off and the resulting ballast-induced moment remains constant.

As shown in Fig. 7a, ballast water is initially distributed evenly among the three variable tanks. When exposed to strong wind (assuming a wind direction of 180°), the FOWT develops an average pitch angle around the *y*-axis due to rotor thrust. In response, the active ballast system automatically adjusts the water distribution among the tanks based on the measured average pitch angle–for example, by transferring water from columns B and C to column A–to maintain platform stability during offshore operation, as illustrated in Fig. 7b.





- (a) Size and position of the ballast tanks
- (b) Equivalent displacement distance of ballast water

Fig. 5. Ballast tank system: (a) Size and position of the ballast tanks; (b) Equivalent displacement distance of ballast water.

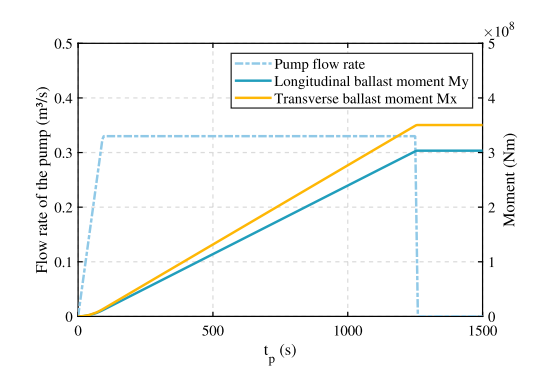


Fig. 6. Ballast pump characteristics.

Table 2 Natural frequencies of FOWT (Hz).

Model	Surge	Heave	Pitch
Present Study	0.007	0.049	0.049
Allen et al. (2020)	0.007	0.037	0.036

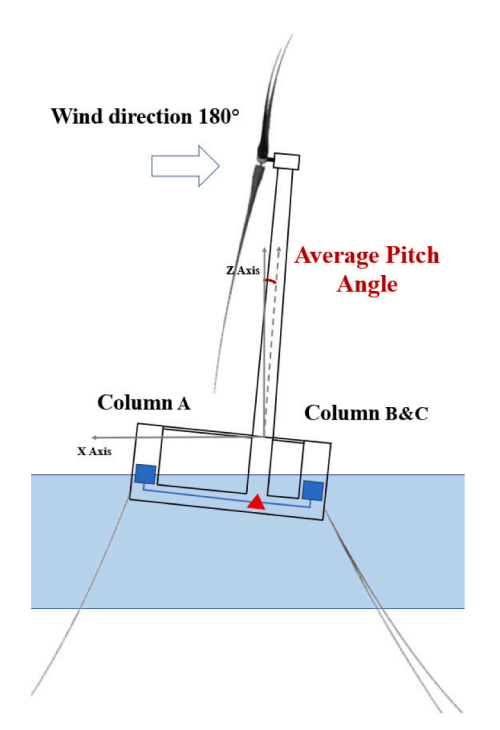
4. Numerical results

4.1. Validation study of coupled method

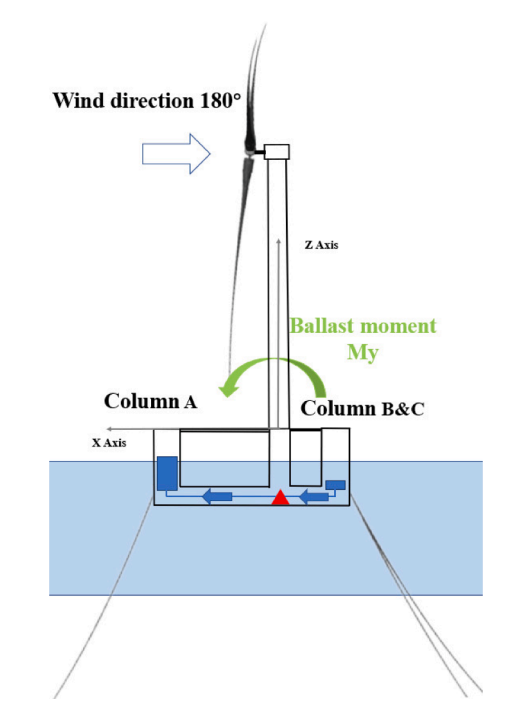
The validity of the selected FOWT model in SESAM is verified through the comparison of hydrodynamic coefficients and free decay simulations. Specifically, the added mass coefficients (A11, A33) and radiation damping coefficients (B11, B33) calculated by WADAM are compared with the simulation results published by Allen et al. (2020). As shown in Fig. 8 and Fig. 9, the x-axis represents wave frequency (Hz), and the y-axis shows the corresponding added mass or damping coefficients. The numerical results demonstrate good agreement with the reference data, confirming the validity of the hydrodynamic computations in the present model. Minor discrepancies may arise from manual extraction of reference data, differences in panel mesh generation, and variations in software for computing hydrodynamic coefficients; however, the overall trends remain consistent.

To further validate the dynamic characteristics of the coupled model, frequency domain hydrodynamic coefficients are imported into the time domain simulation module, and free decay tests in calm water are conducted. Surge, heave, and pitch decay tests are performed by applying initial displacements and releasing the platform to observe its natural response. The simulations yield the natural frequencies and decay behavior for each motion mode. Following published recommendations (Allen et al., 2020), the initial surge displacement is set to 30 m. The simulated surge decay response is compared with the data from Allen et al., showing close agreement, as illustrated in Fig. 10. Table 2 presents the natural frequencies of surge, heave, and pitch motions, along with corresponding values from the reference study, further supporting the validity of the coupled dynamic model.

Ocean Engineering 343 (2026) 123142



W. Meng et al.



- (a) Inclined floating status of the FOWT under wind thrust
- (b) Restored upright floating status after active ballasting

Fig. 7. Schematic of platform attitude adjustment: (a) shows the inclination caused by wind loading, while (b) shows the upright restoration through active ballast transfer.

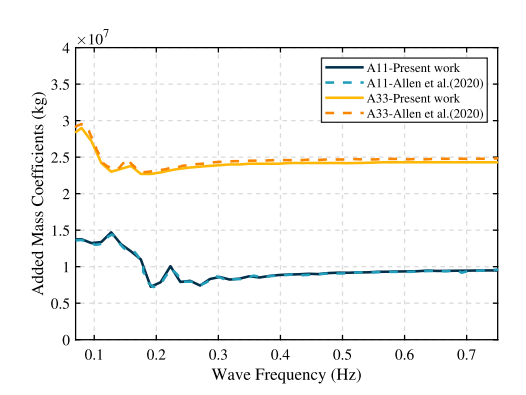


Fig. 8. Comparison of added mass coefficients.

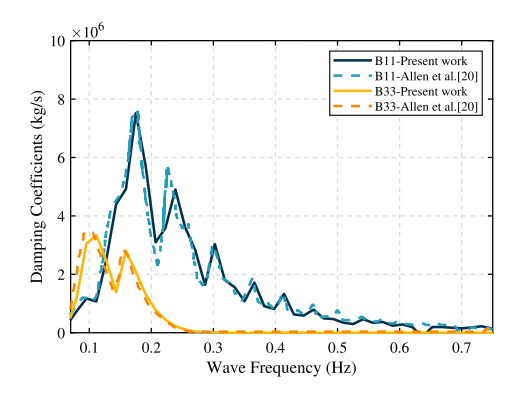


Fig. 9. Comparison of damping coefficients.

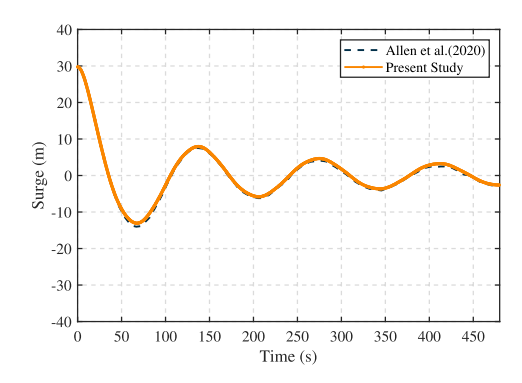


Fig. 10. Comparison of surge free-decay results.

${\it 4.2. \ Verification \ of \ upright-platform \ assumption \ through \ CFD \ simulations}$

To validate the application of the frequency-domain variables in the time-domain simulations (see Eq. (1)), which are computed from the mean wetted surface of the upright platform, two-phase flow simulations are performed using OpenFOAM. A numerical wave tank is built to simulate a series of regular wave cases. Platform inclination is introduced by applying an inclination moment due to rotor thrust, representing the effect of wind loading during turbine operation. The motion responses of the inclined and upright configurations are compared to evaluate the influence of inclination. In addition, Fourier transforms are applied to the time histories of platform motions, and the resulting response amplitudes are compared with Response Amplitude Operators (RAOs) obtained from potential-flow analysis. The following sections detail the CFD model setup, mesh generation, and motion response comparison.

The two-phase flow simulations in the numerical wave tank are conducted using a 1:50 scale model. The mass distribution of the FOWT accounts for major components such as the nacelle and tower.

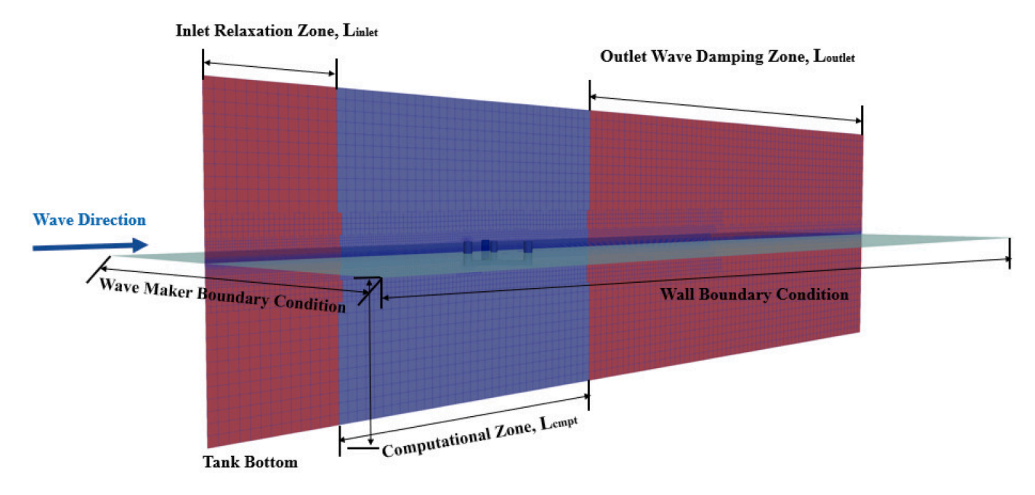


Fig. 11. Simulation Set-up.





(a) CFD simulation of upright-state platform at 15 s

(b) CFD simulation of inclination-state platform at 15 s

Fig. 12. Different floating state of the platform.

Table 3Comparison of full-scale and model-scale FOWT parameters.

Component	Parameter	Value
FOWT	Mass VCG (from base) Roll inertia Pitch inertia Yaw inertia	$2.00 \times 10^7 \text{ kg}$ 17.89 m $3.93 \times 10^{10} \text{ kg m}^2$ $3.93 \times 10^{10} \text{ kg m}^2$ $2.37 \times 10^{10} \text{ kg m}^2$
Model (1:50)	Mass VCG (from base) Roll inertia Pitch inertia Yaw inertia	156.82 kg 0.36 m 122.83 kg m ² 122.83 kg m ² 73.90 kg m ²

A horizontal spring is employed to replace the mooring lines for constraining the floating body, with its horizontal stiffness set identical to that of the original mooring system. This setup enables a focused investigation of the hydrodynamic characteristics induced by platform inclination, while ensuring that the primary emphasis of the study remains on the fluid dynamic effects rather than the specifics of mooring constraints. The scaled values for the center of gravity and moments of inertia of the platform are summarized in Table 3. As shown in Fig. 11, the computational domain has a width of 12 m and a depth of 4 m. The domain is divided into three regions: an inlet relaxation zone, a computational zone, and an outlet damping zone, with lengths of 1λ , 2λ and 5λ , respectively, where λ is the wavelength of the incoming wave. The regular wave conditions used in the simulation are listed in Table 4.

Fig. 12 illustrate the numerical simulation states of the semisubmersible platform under upright and inclined conditions. The inclination angle is set to 5°, reflecting the typical maximum value observed at rated wind speed in both our simulations and the reference design. Our simulations show that the maximum inclination at rated wind speed is about 5° (see Fig. 17(b), case "LC3-A" without active ballast). Similarly, Allen et al. reported in Section 4 (System Performance Assessment) that under both normal turbulence and extreme wind models,

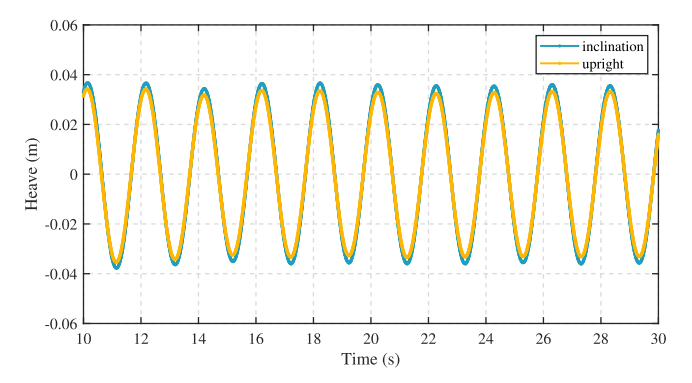
Table 4Wave parameters at full and model scales.

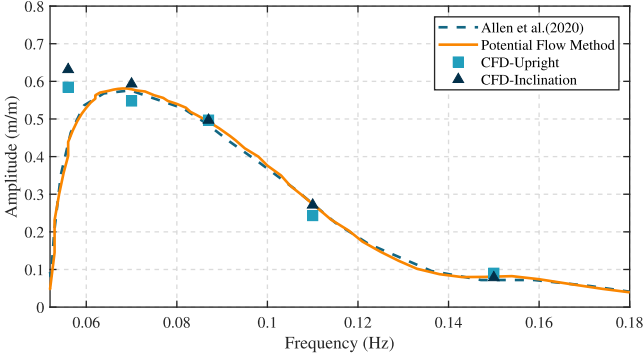
No.	Full Scale		Model Scale (1:50)		
	Frequency (Hz)	λ (m)	Frequency (Hz)	λ (m)	
1	0.05	497.87	0.40	9.95	
2	0.07	318.63	0.50	6.37	
3	0.09	206.28	0.62	4.13	
4	0.11	129.03	0.78	2.58	
5	0.15	69.39	1.06	1.39	

the maximum inclination remains close to 5° and below 6° . In addition, since the adjustment range of the active ballasting system in this study is predefined as -5° to $+5^{\circ}$, we adopted 5° as the target inclination in the CFD simulations to ensure consistency with the control design.

As shown in Fig. 13 and Fig. 14, the time series of the platform motions under regular wave conditions demonstrate only slight variations in amplitude between the two floating states. Similarly, the RAO curves obtained from Fourier-transformed motion responses also show good agreement, indicating that platform inclination has a limited effect on the wave-induced dynamic behavior within the tested range of motion. At low frequencies, the heave amplitude is intrinsically small, so even minor differences may appear visually significant due to the vertical scale in Fig. 13b. Furthermore, potential flow theory and viscous CFD capture hydrodynamic effects differently—particularly in viscous damping and nonlinear effects—which may also contribute to the observed discrepancies. The comparison results between the inclined and upright states reveal that the overall hydrodynamic responses of the platform remain largely consistent across heave and pitch motions.

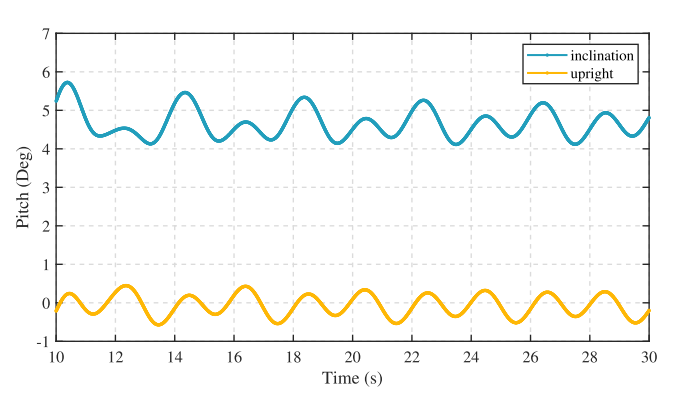
These findings align with conclusions from previous studies. For example, Li et al. (2024a) reported that during the ballast water redistribution process, when the inclination angle of the platform remains below 15°, the hydrodynamic coefficients derived from the upright condition can still be used reliably in numerical simulations. This provides a valuable reference for engineering practice, where high-fidelity CFD simulations under inclined conditions are computationally expensive.

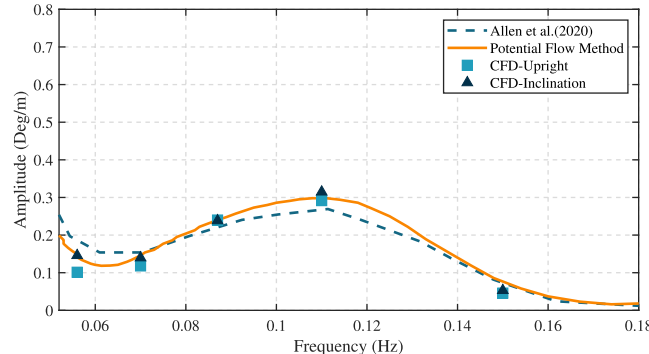




- (a) Comparison of the time series of heave motions of different platform stare at $\lambda = 6.37$ m
- (b) Comparisons of RAO of the heave motion

Fig. 13. Comparisons of heave motion in CFD method.





- (a) Comparison of the time series of pitch motions of different platform stare at $\lambda = 6.37$ m
- (b) Comparisons of RAO of the pitch motion

Fig. 14. Comparisons of the pitch motion in CFD method.

Given that the previous study also observes only minor deviations in motion responses between upright and inclined cases, it is reasonable to proceed with the development and evaluation of the active ballast control strategy based on potential-flow assumptions and upright-state hydrodynamic parameters.

Therefore, the upright configuration under potential-flow theory is considered an acceptable simplification for modeling wave-induced responses when the platform inclination remains within a moderate range. This allows the subsequent study to focus on the control performance of the active ballast system without introducing significant hydrodynamic uncertainty due to inclination effects.

4.3. Simulation cases

Following the reference recommendations (Allen et al., 2020), a subset of the International Electrotechnical Commission (IEC) design load cases (IEC61400, 2005) is selected in this study to evaluate the performance of the FOWT with active ballasting under typical normal operating conditions. For the purpose of validating the coupled simulation method of the active ballast control system, these representative conditions are adopted for the analysis. Table 5 summarizes the details of the selected design load cases. Normal sea states and the normal turbulence model (NTM) are used to simulate environmental conditions. In Table 5, V_{wind} is the mean wind speed in NTM, H_s is the significant wave height and T_p is the peak period. The evaluation covers three critical operational aspects: (1) Load Cases 1-5 assess the ballasting capacity under constant 180° wind-wave misalignment across varying wind speeds, where higher mean wind speed V_{wind} correspond to greater significant wave height H_s ; (2) LC 6–7 examine the adaptability of the

Table 5Simulation cases

Load Case	Wind Type	Wind Direction	Wave Direction	V _{wind} (m/s)	<i>H</i> _s (m)	T_p (s)
LC1-A, LC1-B	NTM	180°	180°	8.00	1.32	8.01
LC2-A, LC2-B	NTM	180°	180°	10.00	1.54	7.65
LC3-A, LC3-B	NTM	180°	180°	10.59	1.63	7.59
LC4-A, LC4-B	NTM	180°	180°	12.00	1.84	7.44
LC5-A, LC5-B	NTM	180°	180°	14.00	2.19	7.46
LC6-A, LC6-B	NTM	90°	90°	10.59	1.63	7.59
LC7-A, LC7-B	NTM	135°	135°	10.59	1.63	7.59
LC8-A, LC8-B	NTM	90°	180°	10.59	1.63	7.59

active ballasting system to directional variations; and (3) LC 8 specifically evaluates the performance under different wind-wave misalignment conditions.

For each environmental condition, simulations are conducted over a 3 h sea state, following the DNVGL-RP-C205 guideline (Dnv, 2017). The initial 200 s are excluded to remove startup transients, consistent with the approach of Kvittem and Moan (2015), so the analysis focuses on the interval from 200 s to 11 000 s. Turbulent wind fields are generated using TurbSim (Jonkman and Buhl, 2006), with the wind field duration matching the total simulation time. Turbulence is generated using the Kaimal spectrum and the IEC normal turbulence model, with a turbulence intensity of 0.12 (Kvittem and Moan, 2015). The wind profile follows a power law with an exponent of 0.14 (IEC61400, 2005). Irregular wave conditions are simulated using the JONSWAP spectrum.

To account for variations in turbulent wind, this study performs two simulations for each load case (LC), as shown in Table 5. For each case,

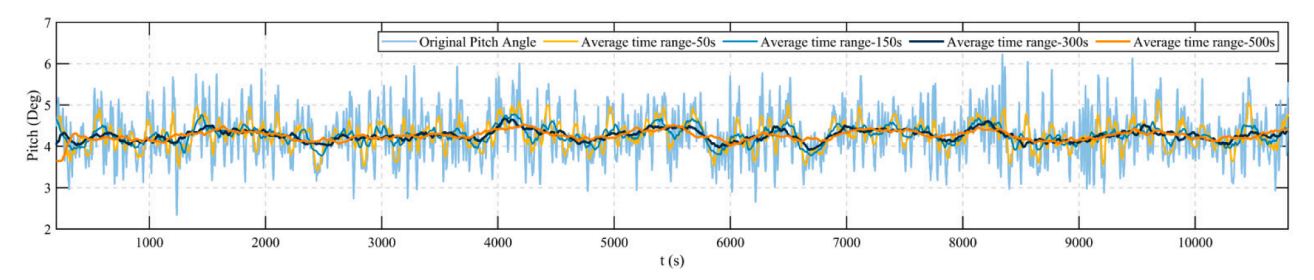


Fig. 15. Comparison of different average time range in LC3 (Direction 180°, $V_{wind} = 10.59 \,\mathrm{m/s}$, $H_s = 1.63 \,\mathrm{m}$, $T_p = 7.59 \,\mathrm{s}$).

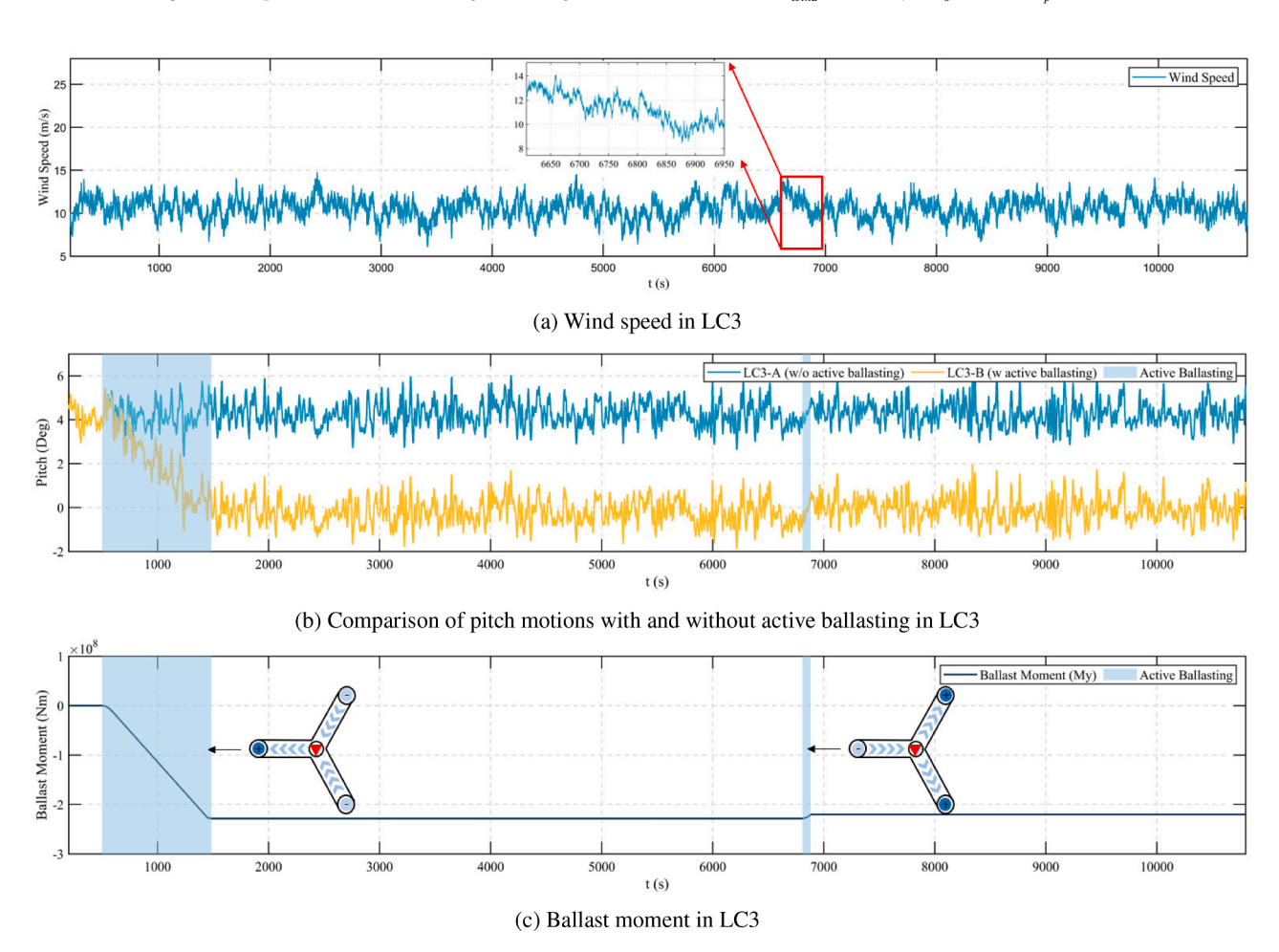


Fig. 16. Comparison of pitch motion and ballast moment in LC3 with/without active ballasting.

the suffix "-A" (e.g., LC1-A) indicates the simulation without the active ballast system, while the suffix "-B" (e.g., LC1-B) indicates the simulation with the active ballast system. The two sets of simulations use identical wind and wave conditions, ensuring a consistent basis for evaluating the impact of the active ballasting system on platform stability.

4.4. Analysis on the platform motions under different loading conditions

Due to the influence of turbulent wind and irregular waves, the pitch and roll angles of the platform exhibit frequent fluctuations. To mitigate the impact of these oscillations, the active ballasting system uses a time-averaged value of the pitch or roll angle over a recent period as the control input. To determine the optimal averaging time window, a comparison is conducted using pitch motion data from LC3-A under rated wind speed conditions, covering the simulation time from 200 s to 11000 s. As shown in Fig. 15, an averaging window of 300 s

provides the best trade-off between measurement stability and control responsiveness.

Fig. 16a presents the wind speed data for wind speeds of $10.59\,\mathrm{m/s}$ in LC3-A and LC3-B, while Fig. 16b illustrates the pitch motion response of the platform under these wind conditions for both configurations. In the legend of Fig. 16b, "w" denotes "with" and "w/o" denotes "without" active ballasting. As shown in the red box of Fig. 16a (between 6600 s and 6900 s), the wind speed decreases steadily for more than 300 s. During this period, the active ballasting system is triggered, resulting in a moderate reduction of the ballast moment, as shown in Fig. 16c. The results demonstrate that following the activation of the active ballasting system, the mean pitch motion gradually returns to near-zero values, indicating effective stabilization of the platform.

Fig. 17 demonstrates the comparison of pitch and roll motion responses and ballast moments under oblique wave conditions (135° wind direction and 135° wave direction). From 500 to 1300 s, the active ballasting system performs a long-duration adjustment based on the aver-

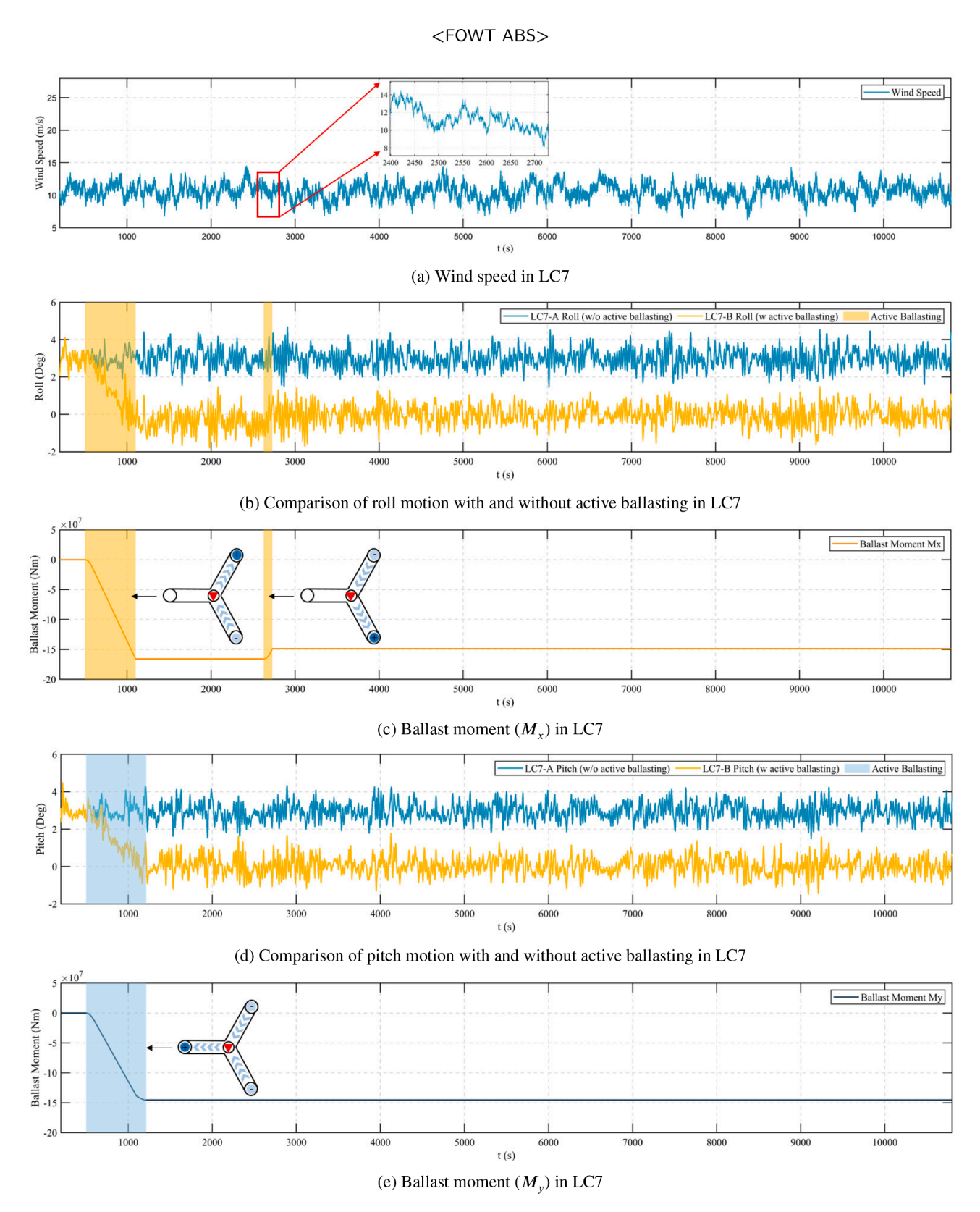


Fig. 17. Comparison of pitch and roll motion and ballast moment in LC7 with/without active ballasting.

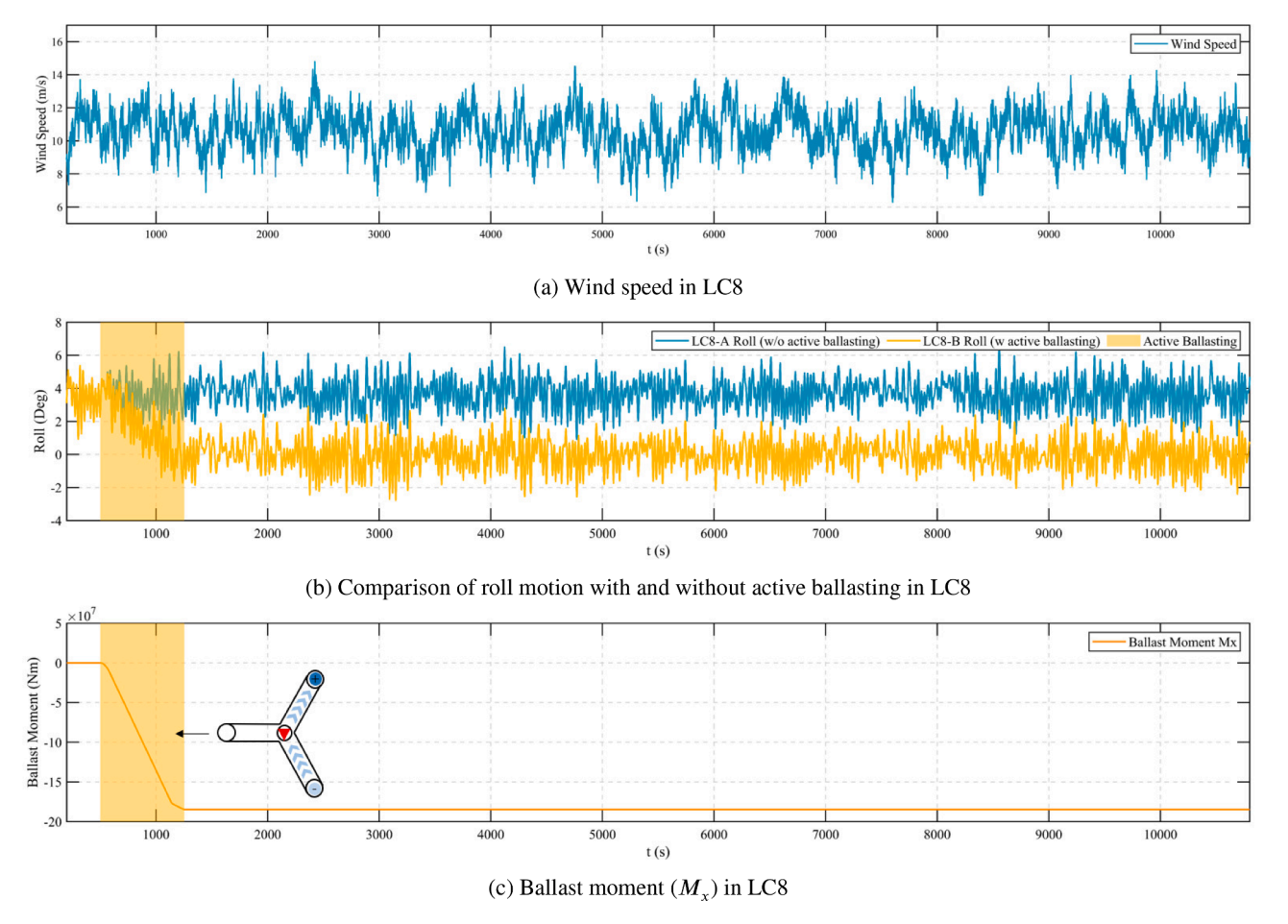


Fig. 18. Comparison of pitch and roll motion and ballast moment in LC8 with/without active ballasting.

age inclination angle, stabilizing both roll and pitch motions near $0^\circ.$ Subsequently, between 2400 and 2700 s, as shown in Fig. 17a, the wind speed continuously drops for more than 300 s, resulting in a decrease in the wind-induced moment. During this period, the average roll angle of the platform reaches approximately $-1^\circ,$ which triggers the active ballasting system. The system then reduces the ballast moment, allowing the roll motion to stabilize around $0^\circ,$ as reflected in Fig. 17c. The results demonstrate the capability of the active ballasting system to stabilize platform motions and minimize oscillations under varying wind and wave conditions.

As shown in Fig. 18, with a 90° wind direction and 180° wave direction, the active ballasting system compensates for the mean roll angle induced by wind thrust, maintaining it near 0° . Meanwhile, the mean pitch of the platform stays close to 0° , indicating that no longitudinal ballast adjustment is required at this time.

These results demonstrate the effectiveness of the active ballasting system in maintaining stability of the platform across different operating conditions. Figs. 16, 17, and 18 collectively illustrate the adaptability of the active ballasting system in regulating the mean inclination angles of the platform under varying wind-wave misalignment conditions.

In the present study, while the turbulent wind exhibits fluctuations, its mean speed remains essentially constant. The active ballasting system performs a single prolonged adjustment, typically completed around 1500 s. During the three-hour simulation, the 300 s moving average wind speed still shows variations. By optimizing the derivative coefficient (Kd) in the PID controllers, the impact of these fluctuations was mitigated, thereby minimizing both the subsequent adjustment duration and frequency. As evident from Fig. 16, Fig. 17 and Fig. 18, the total ballasting time is effectively controlled within approximately 20 minutes

over the three-hour period while maintaining the mean pitch motion of the platform near 0° .

To further quantify the effectiveness of the active ballasting system, statistical analyses are conducted for the time interval between 1500 s and 11 000 s after the completion of the primary ballast adjustment. This evaluation focuses on the average, maximum, and minimum of platform motions under various environmental conditions. The statistical results from Fig. 19 to Fig. 24 demonstrate the effectiveness of the active ballasting system in reducing the mean inclination of the platform across a range of operating conditions.

As shown in Fig. 19, the average pitch angle in the cases with active ballasting remains consistently close to 0° across all tested wind speeds, indicating that the platform maintains an upright posture. In contrast, the cases without ballasting exhibit average pitch angles of approximately 3° to 4°, with noticeably higher maximum values. These results confirm that the active ballasting system effectively suppresses pitch inclination and stabilizes the platform under varying turbulent wind conditions.

Fig. 20 shows that the surge motion exhibits little change between the two cases, indicating that the ballasting system has limited influence on the horizontal translational motion. Similarly, as shown in Fig. 21, the heave response is largely unaffected by the ballast adjustment, which is expected as the system primarily targets restoring moments in the pitch and roll directions rather than vertical motion.

Figs. 22,23,24 further demonstrate the robustness of the control strategy under various wind-wave misalignment conditions. Under aligned (90°), oblique (135°), and cross-sea (180°) conditions, the mean pitch and roll angles are consistently reduced in the presence of active ballast control. For example, in Fig. 25, the maximum roll angle without

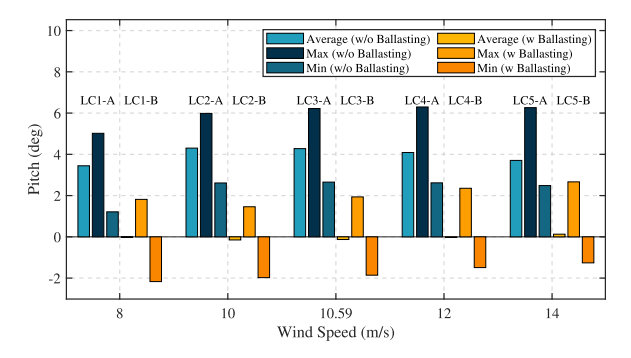


Fig. 19. Statistical data of pitch motion with/without active ballast under different wind speeds.

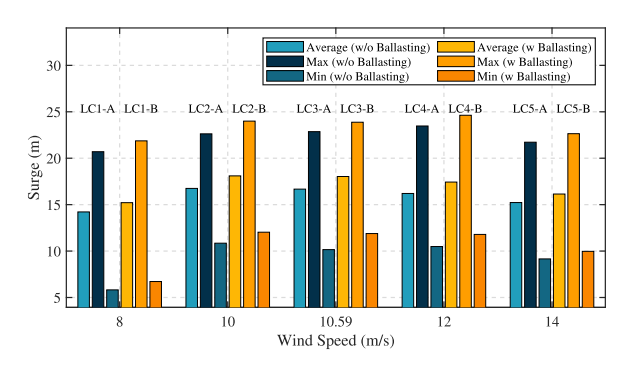


Fig. 20. Statistical data of surge motion with/without active ballast under different wind speeds.

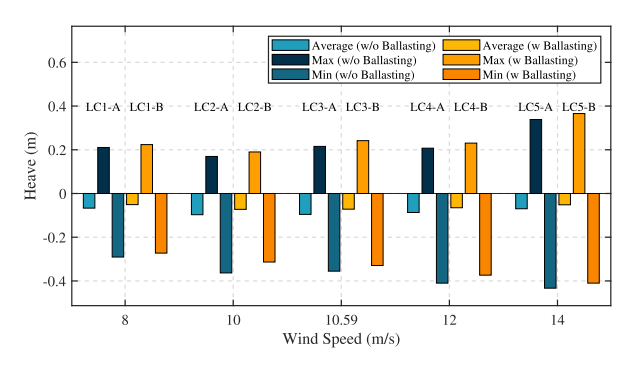


Fig. 21. Statistical data of heave motion with/without active ballast under different wind speeds.

ballast reaches over 6° , whereas with ballasting, it is maintained within $\pm\,3^\circ$. Similar trends are observed for pitch motion.

In summary, the proposed active ballasting system effectively reduces the steady-state inclination of the floating platform under complex environmental conditions, although its influence on surge and heave motions remains limited.

4.5. Analysis on electrical generator output under different loading conditions

Figs. 25 to 28 compare the electrical generator performance of the FOWT under various load conditions, highlighting the impact of active ballast adjustment on power output, platform motion, and rotor thrust.

As shown in Fig. 25a, under LC3 conditions, the power output with active ballasting (LC3-B) consistently exceeds that of the case without ballast adjustment (LC3-A), particularly during peak production phases. Although the thrust in LC3-B is slightly higher, this reflects improved aerodynamic loading due to enhanced platform stability. Fig. 25b fur-

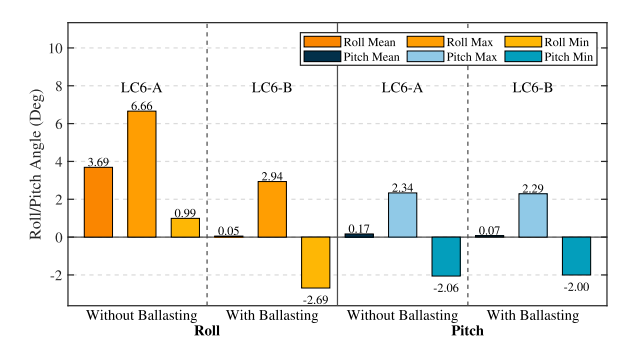


Fig. 22. Statistical data of motions with/without active ballast under aligned wind and wave (90°) at rated wind speed.

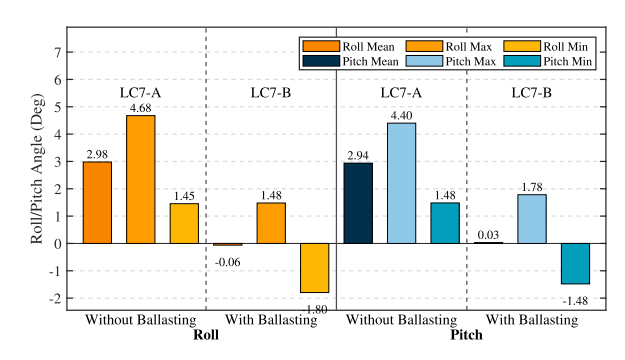


Fig. 23. Statistical data of motions with/without active ballast under oblique wind and wave (135°) at rated wind speed.

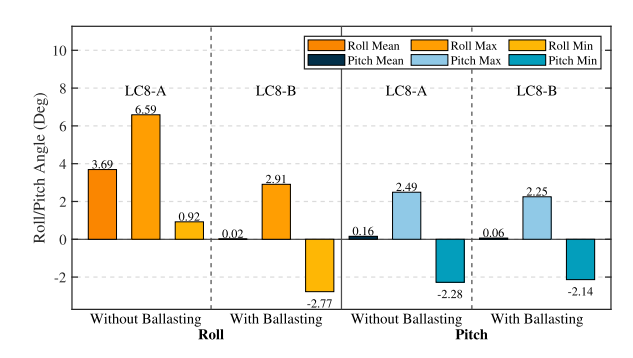
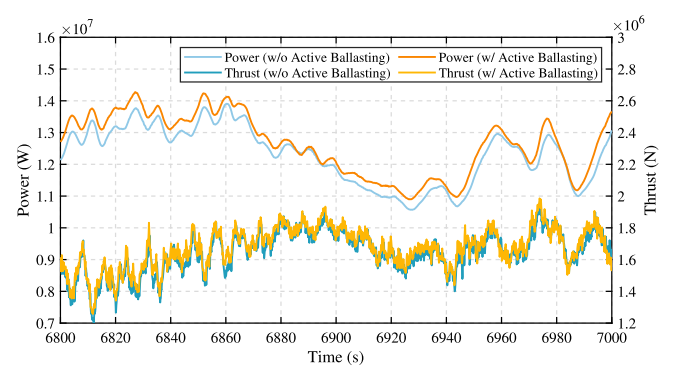


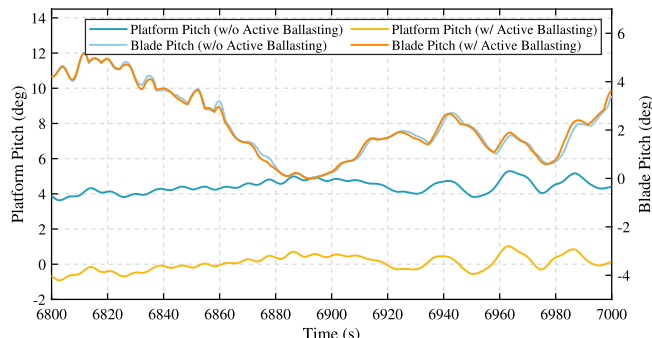
Fig. 24. Statistical data of motions with/without active ballast under cross sea condition (wind 90°, wave 180°) at rated wind speed.

ther demonstrates that LC3-B maintains a lower and more stable pitch angle, resulting in reduced blade pitch fluctuations.

Similar trends are observed under LC7 (Fig. 26a and Fig. 26b), where the application of active ballast results in both increased generator output and reduced platform inclination. The platform motion stabilization leads to smoother blade pitch control, contributing to more consistent aerodynamic efficiency.

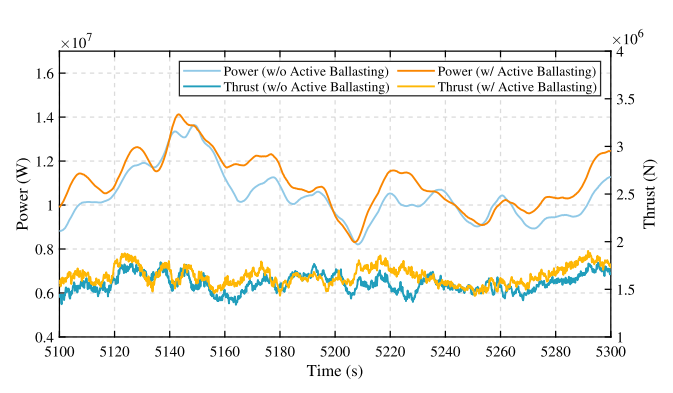
Figs. 27 and 28 present the average generator output under different wind speeds and wind-wave misalignment conditions. In all cases, the use of active ballasting yields higher average power. Specifically, Fig. 27 shows an increase of up to 2.76% at 10.59 m/s, while Fig. 28 shows improvements of around 2.4–2.7% across all tested wind-wave angles. These results confirm that the active ballasting system enhances energy production by mitigating inclination-induced aerodynamic losses. In addition, during FOWT operation, excessive platform inclination may prompt operators to shut down the turbine to ensure safety, resulting in zero power output. In such cases, the active ballasting system plays a critical role by maintaining the mean platform inclination close to 0°, thereby reducing downtime caused by excessive inclination. This not

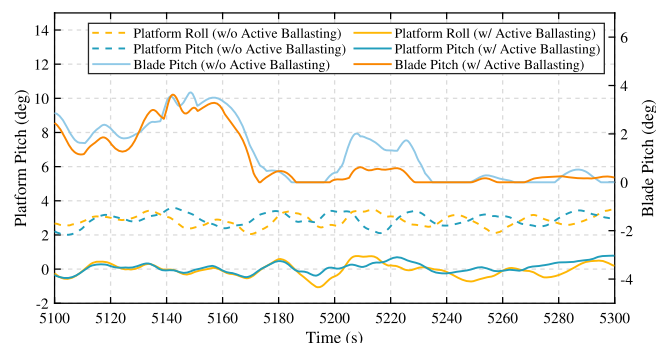




- (a) Comparison of power outputs and thrust with/without active ballast in LC3
- (b) Comparison of platform motion and blade pitch angle with/without active ballast in LC3

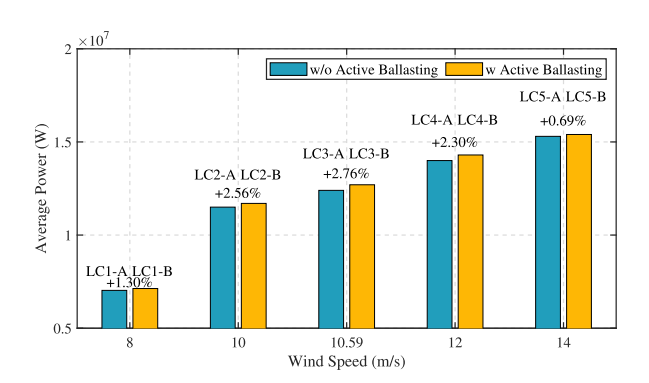
Fig. 25. Comparison of electrical generator performance in LC3.

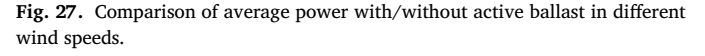




- (a) Comparison of power outputs and thrust with/without active ballast in LC7
- (b) Comparison of platform motion and blade pitch angle with/without active ballast in LC7

Fig. 26. Comparison of electrical generator performance in LC7.





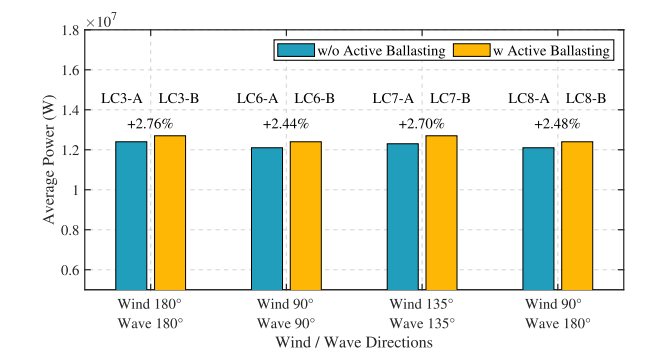


Fig. 28. Comparison of average power with/without active ballast in different wind and wave directions.

only ensures safe and stable operation but also offers potential benefits in mitigating structural fatigue (Gao et al., 2024).

The baseline ROSCO controller (Abbas et al., 2022) typically initiates blade pitch control to limit thrust and maintain stability when large platform motions are detected. However, with the active ballasting system in operation, platform motions are significantly reduced, thereby limiting the need for aggressive blade pitch control. This contributes to more consistent thrust and power output, enhancing overall energy capture efficiency.

4.6. Analysis on the mooring forces under different loading conditions

Figs. 29,30,31,32 compare the axial forces of the three mooring lines with and without active ballast adjustment under different environmental load cases. Mooring lines are numbered according to Fig. 4, with mooring line 1 oriented in the 180° direction.

In LC3 (180° aligned wind and wave), mooring line 1 exhibits the highest axial force, ranging between 3.6-4.8 MN. Mooring lines 2 and 3 remain in the range of 2.0–2.5 MN, and show limited response to ballast adjustment. A similar trend is observed under LC6 (cross wind), LC7 (oblique wind-wave), and LC8 (cross sea state), where mooring line 1 consistently bears the highest load due to its alignment with the primary wave direction. Active ballast adjustment has minimal influence on the

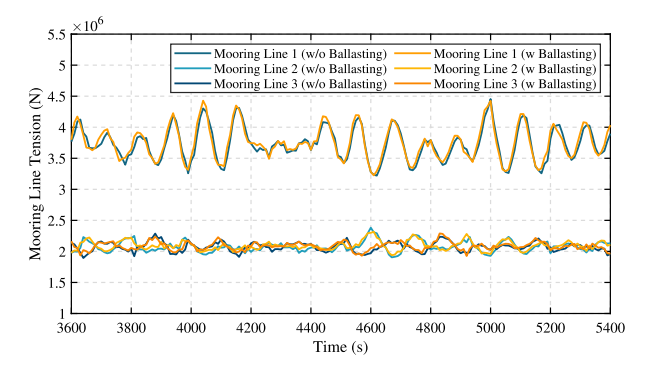


Fig. 29. Comparison of the axial force of mooring lines with/without active ballasting in LC3.

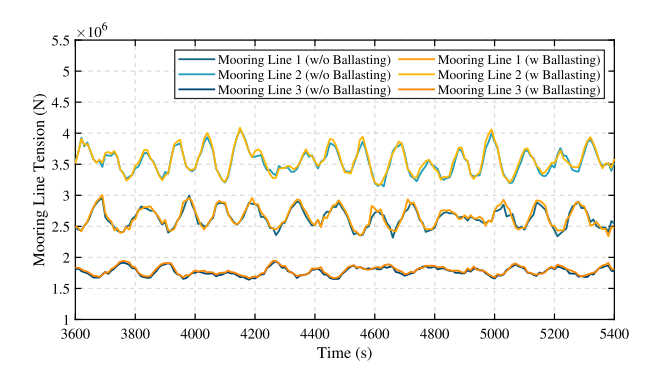


Fig. 30. Comparison of the axial force of mooring lines with/without active ballasting in LC6.

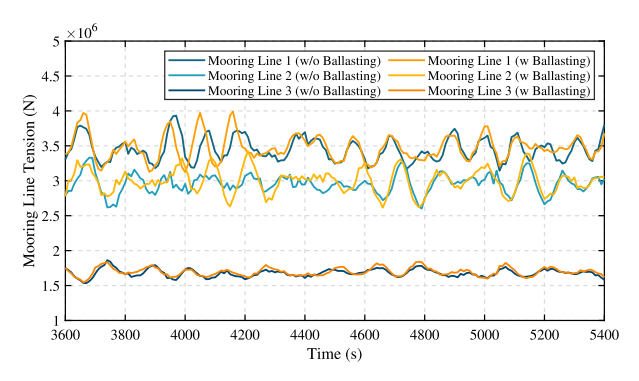


Fig. 31. Comparison of the axial force of mooring lines with/without active ballasting in LC7.

amplitude and phase of tension oscillations across all lines and load cases.

Figs. 33, 34, and 35 present statistical comparisons of mean, maximum, and minimum axial tensions of the mooring lines under turbulent wind speeds ranging from 8 to 14 m/s in the 180° wind-wave alignment condition. Across all wind speeds, mooring line 1 maintains the highest average tension, reaching up to 4.0 MN, while lines 2 and 3 remain below 2.5 MN. As also reflected in the surge motion trends in Fig. 20, the mean, maximum, and minimum tensions of mooring 1 all increase with larger surge amplitudes. Mooring-line tensions are mainly governed by platform horizontal motions and are only weakly affected by platform inclination. Since the active ballasting system primarily adjusts pitch and roll angle, its effect on mooring tensions is negligible, and the original mooring configuration can be retained after its implementation.

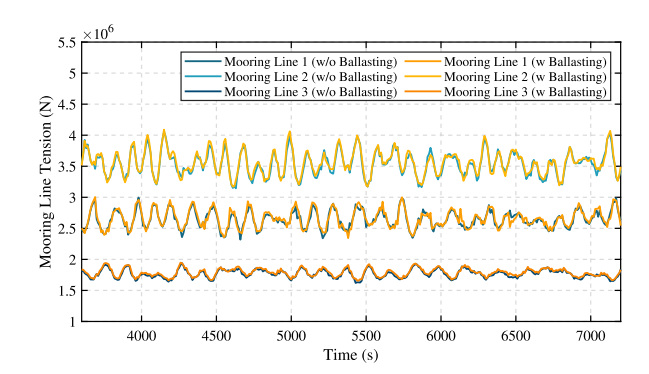


Fig. 32. Comparison of the axial force of mooring lines with/without active ballasting in LC8.

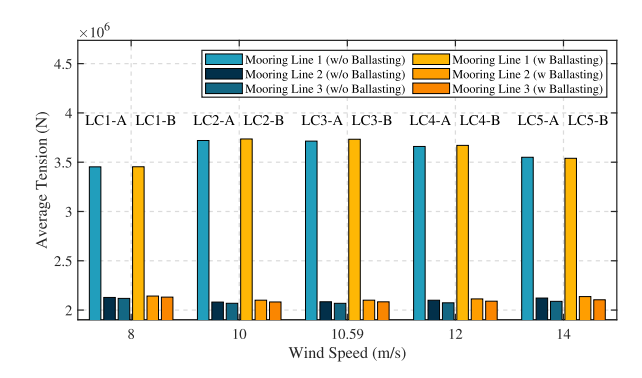


Fig. 33. Average tension of the mooring lines with/without active ballast in 180° direction under different wind speeds.

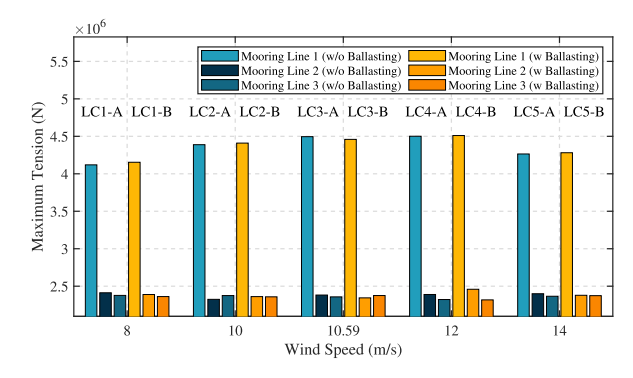


Fig. 34. Maximum tension of the mooring lines with/without active ballast in 180° direction under different wind speeds.

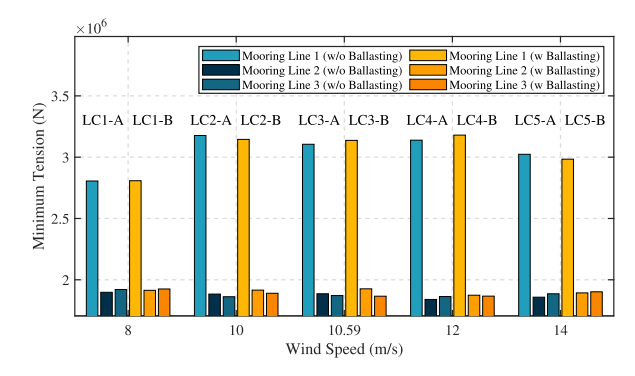


Fig. 35. Minimum tension of the mooring lines with/without active ballast in 180° direction under different wind speeds.

Overall, the results demonstrate that while active ballast adjustment effectively regulates platform inclination, it does not significantly alter the tension distribution in the mooring system. Mooring line 1, aligned with the wave-heading direction, continues to function as the dominant load-bearing line, with lines 2 and 3 providing lateral constraint and balance.

5. Conclusion and future work

In this study, an analysis model considering the aero-hydro-mooring coupling and active ballasting system is developed using SESAM software. Interaction between the FOWT and the active ballasting system is facilitated via the Python interface in SESAM and the TCP communication protocol. The IEA 15 MW floating wind turbine is selected as the reference model for this study. Additionally, CFD simulations are performed to investigate the hydrodynamic responses of the platform under both upright and inclined conditions, confirming the accuracy of the upright platform assumption for potential-flow simulations. Time-domain simulations are then conducted under various operating conditions, with the active ballasting system dynamically adjusting the ballast moments based on the platform average pitch and roll motion using a PID control algorithm.

The results indicate that the active ballasting system significantly reduces the maximum inclination angle of the platform by dynamically adjusting ballast water. Its effectiveness has been evaluated under various wind and wave directions. After ballast water adjustment, the average inclination angles approach zero, while the maximum inclination amplitude is substantially reduced in turbulent wind conditions, enhancing operational safety and stability. In terms of power generation, the comparison of the power generation time history curves shows that after the active ballasting system is activated, the power output increases at the same time. Statistically, this leads to a 2.76 % rise in the average power output near the rated wind speed of 10.59 m/s and reduces the blade pitch control, resulting in more consistent energy production. In the operation of FOWTs, when the platform inclines significantly (roll or pitch angles exceed 5°), the wind power operation enterprise may shut down to ensure safety, resulting in zero power output. In such cases, the active ballasting system plays a critical role by maintaining the mean inclined angles of the platform close to 0°, preventing excessive incline. This minimizes downtime, enhances power generation efficiency, and ensures the safe and stable operation of the equipment. As for mooring performance, the forces on all mooring lines remain stable before and after ballast adjustment, as mooring tensions are mainly influenced by platform horizontal motions rather than roll and pitch motions. Since the active ballast system regulates roll and pitch motions with little effect on line tensions, the existing mooring configuration requires no modification after its integration.

The study provides a framework for coupling and analyzing FOWTs with active ballasting systems under turbulent wind conditions. Future research will focus on applying advanced control strategies, such as Model Predictive Control (MPC), to further optimize the performance of the active ballasting system. This will aim to enhance its adaptability, responsiveness, and efficiency across a wider range of operational scenarios, including rapid load changes and varying sea states. The integration of such predictive control approaches is expected to enable more precise ballast adjustments, improve platform stability, and reduce structural fatigue under dynamic environmental conditions.

In parallel, the present framework will be extended into a coupled CFD environment to investigate the hydrodynamic interactions between the platform and its ballast tanks. An active ballasting model will be implemented in CFD, with the controller prescribing tank inflows and outflows as dynamic boundary conditions and sloshing-induced forces fed back in real time. As high-fidelity blade-airflow simulations remain prohibitively expensive, aerodynamic loads will instead be modeled using BEM and transferred to the platform via AeroDyn-OpenFOAM coupling. This hybrid strategy will ensure computational efficiency while captur-

ing transient ballast-water effects, platform-sloshing coupling, and system performance in extreme wave conditions.

Declaration of competing interest

The authors declare that they have no known competing financial interests or personal relationships that could have appeared to influence the work reported in this paper.

Acknowledgement

The work is supported by the National major science and technology project for new oil and gas exploration and development "Oil & Gas Major Project" (Grant No. 2024ZD1403301).

CRediT authorship contribution statement

Wei Meng: Writing – review & editing, Supervision, Resources, Conceptualization; Jiacan Lyu: Writing – original draft, Methodology; Yao Zhang: Writing – review & editing, Methodology; Shangmao Ai: Validation; Huanfeng Song: Resources.

References

- Abbas, N.J., Zalkind, D.S., Pao, L., Wright, A., 2022. A reference open-source controller for fixed and floating offshore wind turbines. Wind Energy Sci. 7, 53–73. https://doi. org/10.5194/wes-7-53-2022
- Allen, C., Viscelli, A., Dagher, H., Goupee, A., Gaertner, E., Abbas, N., Hall, M., Barter, G., 2020. Definition of the UMaine VolturnUS-S reference platform developed for the IEA wind 15-megawatt offshore reference wind turbine. Technical Report. Technical Report. https://doi.org/10.2172/1660012
- Amaral, G.A., Mello, P.C., Carmo, L. H. S.D., Alberto, I.F., Malta, E.B., Simos, A.N., Franzini, G.R., Suzuki, H., Gonçalves, R.T., 2021. Seakeeping tests of a fowt in wind and waves: an analysis of dynamic coupling effects and their impact on the predictions of pitch motion response. J. Mar. Sci. Eng. 9. https://doi.org/10.3390/jmse9020179
- Antonutti, R., Peyrard, C., Johanning, L., Incecik, A., Ingram, D., 2016. The effects of wind-induced inclination on the dynamics of semi-submersible floating wind turbines in the time domain. Renew. Energy 88, 83–94. https://doi.org/10.1016/j.renene.2015.11.
- Bara, C., Cornoiu, M., Popescu, D., 2012. An optimal control strategy of ballast systems used in ship stabilization. IEEE. Th Mediterranean conference on control & automation (MED). https://doi.org/10.1109/MED.2012.6265749
- Cai, X., Zhang, H., 2021. Stability study of floating wind turbine based on tmd control. J. Hehai Univ. (Nat. Sci.) 49, 70–76. https://doi.org/10.3876/j.issn.1000-1980.2021. 01.011
- Dalzell, J.F., 1976. Application of the functional polynomial model to the ship added resistance problem. In: Published by Stevens Institute of Technology, 11Th Symposium on Naval Hydrodynamics.
- Deshpande, S.S., Anumolu, L., Trujillo, M.F., 2012. Evaluating the performance of the two-phase flow solver interfoam. Computat. Sci. Discov. 5. 014016. https://doi.org/ 10.1088/1749-4699/5/1/014016
- Dnv, 2017. Environmental conditions and environmental loads, Recommend Practice DNVGL-RP-C.
- Dnv, 2023a. Oslo, Norway. RIFLEX 4.16 Theory Manual, 4.16 ed. Released version.
- Dnv, G., 2019. Coupled analysis of floating wind turbines. In: Recommend Practice DNVGL-RP-0286.
- Dnv, S., 2023b. Oslo, Norway. 24 Theory Manual, 4.24 ed. Released version.
- Dnv, S., Manual, W.U., 2023. Wave analysis by diffraction and morison theory. DNV 10. 3rd ed. released version.
- Dou, P., Wang, Z., Ling, H., Xu, X., 2023. Motion control of a multi-layer multi-modal platform structure with a tuned liquid damper. J. Vibrat. Shock 42, 30–39. https:// doi.org/10.13465/j.cnki.jvs.2023.14.004
- Edwards, E.C., Holcombe, A., Brown, S., Ransley, E., Hann, M., Greaves, D., 2023. Evolution of floating offshore wind platforms: a review of at-sea devices. Renew. Sustain. Energy Rev. 183. 113416. https://doi.org/10.1016/j.rser.2023.114271
- Eriksen, R., Engel, D., Haugen, U., 2024. Technical Report. Technology progress report. Energy transition outlook 2024.
- Feng, X., Fang, J., Lin, T., Chen, B., Li, D., Liu, H., Gu, Y., 2023. Coupled aero-hydromooring dynamic analysis of floating offshore wind turbine under blade pitch motion. Phys. Fluids 35. https://doi.org/10.1063/5.0141237
- Gaertner, E., Rinker, J., Sethuraman, L., Zahle, F., Anderson, B., Barter, G., Abbas, N., Meng, F., Bortolotti, P., Skrzypinski, W., Scott, G., Feil, R., Bredmose, H., Dykes, K., Shields, M., Allen, C., Viselli, A., . IEA wind TCP task 37: definition of the IEA 15-megawatt offshore reference wind turbine. Technical Report. National Renewable Energy Lab.(NREL). Golden, CO (United States. https://doi.org/10.2172/1603478
- Gao, Y., Zhai, E., Li, S., Zhang, Z., Xu, Z., Zhang, G., Racic, V., Chen, J., Wang, L., Zhang, Z., 2024. Integrated design and real-world application of a tuned mass damper (tmd) with displacement constraints for large offshore monopile wind turbines. Ocean Eng. 292. 116568. https://doi.org/10.1016/j.oceaneng.2023.116568

Ocean Engineering 343 (2026) 123142

- Grant, E., Johnson, K., Damiani, R., Stockhouse, D., Dinius, J., Phadnis, M., Pao, L., . Combined low-bandwidth platform actuation and floating feedback control for an offshore wind turbine with an ultraflexible substructure. In: 2022 American Control Conference (ACC). IEEE, p. 2022. https://doi.org/10.23919/ACC53348.2022.9867302
- Haider, R., Li, X., Wei, S., Lin, Z., Xiao, Q., Zhao, H., 2024. Review of computational fluid dynamics in the design of floating offshore wind turbines. Energies 17. https: //doi.org/10.3390/en17174269
- Hasselmann, K., 1966. On nonlinear ship motions in irregular waves. J. Ship Res. 10. 64–68.10.5957/isr.1966.10.1.64
- He, E., Xiong, B., Yang, J., 2020. Study on active-passive integrated vibration control of offshore floatingwind turbine based on tmd-hmd. J. Mech. Eng. 56, 73–79. https://doi.org/10.3901/JME.2020.03.073
- Horno, L.D., Somolinos, J.A., Segura, E., Morales, R., 2020. A new proposal for the closed-loop orientation control of a windfloat turbine system. J. Mar. Sci. Eng. 9. https://doi.org/10.3390/JMSE9010026
- Hu, L., Zhang, M., Gong, Q., Bi, J., Gao, M., 2023. Research on ship roll motion control method based on mpc. Chinese J. Hydrodyn. 38, 551–557. https://doi.org/10.16076/ j.cnki.cjhd.2023.04.007
- IEC61400, 61400-1: Wind turbines part 1: Design requirements 177. https://doi.org/10. 1088/1742-6596/75/1/012075, 2005.
- Issa, R., 1986. Solution of the implicitly discretised fluid flow equations by operator-splitting. J. Comput. Phys. 62, 40–65. https://doi.org/10.1016/0021-9991(86) 90099-9
- Jasak, H., 1996. Error Analysis and Estimation for the Finite Volume Method With Applications to Fluid Flows. Technical Report. University of London and Imperial College London. Ph.D. thesis. https://doi.org/10.1016/0148-9062(95)99577-K
- Jasak, H., Tuković, Ž, 2010. Dynamic mesh handling in openfoam applied to fluidstructure interaction simulations. In: Proceedings of the v European Conference on Computational Fluid Dynamics ECCOMAS CFD 2010.
- Jonkman, B.J., Buhl, M. L.J., 2006. TurbSim user's guide. Technical Report. National Renewable Energy Lab.(NREL). https://doi.org/10.2172/15020326
- Kurniawan, A., Hardianto, Koenhardono, , E.S., Kusuma, I.R., 2015. Modeling and control of ballast system to improve stability of catamaran boat. In: 2015 International Conference on Advanced Mechatronics, Intelligent Manufacture, and Industrial Automation (ICAMIMIA). IEEE. https://doi.org/10.1109/ICAMIMIA.2015.7508032
- Kvittem, M.I., Moan, T., 2015. Time domain analysis procedures for fatigue assessment of a semi-submersible wind turbine. Mar. Struct. 40, 38–59. https://doi.org/10.1016/j. marstruc.2014.10.009
- Li, C., Chen, P., Deng, S., Wang, S., Cheng, Z., Xiao, L., 2024a. Effects of ballast transfer on modeling and dynamic responses of a 15mw semi-submersible floating wind turbine. Ocean Eng. 302. 117581. https://doi.org/10.1016/j.oceaneng.2024.117581
- Li, H., Peng, J., Zheng, J., Zhang, J., Peng, W., Zhang, X., 2024b. Influence of heave plates on dynamic responses of a semisubmersible wind turbine. Chinese J. Hydrodyn. 39, 500–508. https://doi.org/10.16076/j.cnki.cjhd.2024.04.004
- Liu, A.Y., Su, S., Chen, J., Yu, H., Duggal, A., Kolb, J.A., 2023. Evaluation of a 15 mw turret moored floating offshore wind turbine. In: Offshore Technology Conference. https://doi.org/10.4043/32415-MS
- Liu, Y., Zhao, X., Wu, D., Li, D., Li, X., 2015. Study on the control methods of a water hydraulic variable ballast system for submersible vehicles 108, 648–661. https://doi. org/10.1016/j.oceaneng.2015.08.045
- Lopez-Pavon, C., Souto-Iglesias, A., 2015. Hydrodynamic coefficients and pressure loads on heave plates for semi-submersible floating offshore wind turbines: a comparative analysis using large scale models. Renew. Energy 81. 864–881.10.1016/j.renene.2015.04.003

- Mahfouz, M.Y., Molins, C., Trubat, P., Hernández, S., Vigara, F., Pegalajar-Jurado, A., Bredmose, H., Salari, M., 2021. Response of the international energy agency (iea) wind 15 mw windcrete and activefloat floating wind turbines to wind and second-order waves. Wind Energy Sci. 6, 867–883. https://doi.org/10.5194/wes-2021-11
- Manwell, J.F., Mcgowan, J.G., Rogers, A.L., 2010. Wind energy explained: theory, design and application. John Wiley & Sons. https://doi.org/10.1002/9781119994367
- Manzi, M., Soltani, B., Guerlain, S., Antonello, P., Queres, J., Gomes, J.O., 2005. Designing a ballast control system operator interface, in: 2005 IEEE Design Symposium, Systems and Information Engineering. IEEE. https://doi.org/10.1109/SIEDS.2005.193264
- Nanos, E.M., Letizia, S., Clemente, D., Wang, C., Rotea, M., Iungo, V., Bottasso, C.L., 2020.
 Vertical wake deflection for offshore floating wind turbines by differential ballast control. IOP Publishing. https://doi.org/10.1088/1742-6596/1618/2/022047
- Newman, J.N., 1974. Second-order slowly varying forces on vessels in irregular waves.
 In: Proceedings of the International Symposium on Dynamics of Marine Vehicles and Structures in Waves.
- Roddier, D., Cermelli, C., Aubault, A., Weinstein, A., 2010. Windfloat: a floating foundation for offshore wind turbines. J. Renew. Sustain. Energy 2. https://doi.org/10.1063/
- Samyn, L.M., Paulo, J., Cunha, V.S., 2009. Dynamic model of a semi-submersible platform for the development of ballast control systems. IFAC Proc. Vol. 42, 146–151. https://doi.org/10.3182/20090916-3-BR-3001.0067
- Santos, C.R., Abdelmoteleb, S.E., Mendoza, A. S.E., Bachynski-Polić, E.E., 2022. Control considerations for very large floating wind turbines 55, 166–171. https://doi.org/10. 1016/j.ifacol.2022.10.426
- Tetteh, E.Y., Fletcher, K., Qin, C., Loth, E., Damiani, R., 2022. Active ballasting actuation for the spiderfloat offshore wind turbine platform. In: AIAA SCITECH 2022 Forum. https://doi.org/10.2514/6.2022-2161
- Wang, Y., Zhou, S., Wen, B., Tian, X., Peng, Z., Ni, Y., Jiang, Y., Zhang, H., 2023. Review of motion suppression methods for floating wind turbines. China Offshore Platform 38, 18–26. https://doi.org/10.12226/j.issn.1001-4500.2023.04.20230403
- Wen, B., Dong, X., Tian, X., Peng, Z., Zhang, W., Wei, K., 2018. The power performance of an offshore floating wind turbine in platform pitching motion. Energy 154, 508–521. https://doi.org/10.1016/j.energy.2018.04.140
- Xue, M., Dou, P., Zheng, J., Lin, P., Yuan, X., 2022. Pitch motion reduction of semisub-mersible floating offshore wind turbine substructure using a tuned liquid multicolumn damper. Mar. Struct. 84. https://doi.org/10.1016/j.marstruc.2022.103237
- Yu, W., Cheng, P.W., Lemmer, F., Lehmann, K., Guzmán, S.D., Moreu, J., Battistella, T., 2022. Model test and validation of the crown floating offshore wind turbine. In: International Conference on Offshore Mechanics and Arctic Engineering. American Society of Mechanical Engineers. https://doi.org/10.1115/OMAE2022-81065
- Zhang, H., Wen, B., Tian, X., Li, X., Dong, Y., Wang, M., Peng, Z., 2023. Experimental study on mitigating vibration of floating offshore wind turbine using tuned mass damper. Ocean Eng. 288. 115974. https://doi.org/10.1016/j.oceaneng.2023.115974
- Zhang, J., Wang, J., Li, H., Wang, F., 2025. Research progress on pitching and pitching suppression of floating wind turbines. J. Hehai Univ. (Nat. Sci.) 53, 103–110. https://doi.org/10.3876/j.issn.1000-1980.2025.01.013
- Zhang, Z., eg, C.H., 2020. Dynamics and control of spar-type floating offshore wind turbines with tuned liquid column dampers. Struct. Control Health Monitor. 27. https://doi.org/10.1002/stc.2532
- Zhao, X., Liu, Y., Han, M., Wu, D., Li, D., 2016. Improving the performance of an auv hovering system by introducing low-cost flow rate control into water hydraulic variable ballast system. Ocean Eng. 125, 155–169. https://doi.org/10.1016/j.oceaneng.2016.08.001